minerals

MDPI

Article

Lithofacies and Pore Structures of the Permian Qixia Dolostone Reservoirs (Central Sichuan Basin, China): Implication of Hydrothermal Dolomitization on Reservoir Quality

Xingyu Zhang [1], Haizhou Qu [2,*], Lianjin Zhang [3], Xiugen Fu [1], Ziye Lu [2], Dongfan Yang [3], Huilin Xu [3] and Yunfeng Zhang [2]

[1] School of Geoscience and Technology, Southwest Petroleum University, Chengdu 610500, China; zhangxingyu0649@163.com (X.Z.); fuxiugen@126.com (X.F.)
[2] SILKROAD Research Center of Oil & Gas Geology and Exploration, Southwest Petroleum University, Chengdu 610500, China; luziyei88@163.com (Z.L.); zhyf@swpu.edu.cn (Y.Z.)
[3] Research Institute of Exploration and Development, PetroChina Southwest Oil and Gas Field Company, Chengdu 610051, China; zhanglianjin268@petrochina.com.cn (L.Z.); ydongfan@petrochina.com.cn (D.Y.); xuhuilin@petrochina.com.cn (H.X.)
* Correspondence: quhaizhou@swpu.edu.cn

Abstract

The Permian Qixia dolostone in the Central Sichuan Basin is a significant hydrocarbon reservoir of hydrothermal origin, linked to the Emeishan Large Igneous Province and structurally controlled by E–W strike–slip faults. However, how this process controls reservoir quality remains poorly understood. To address this, we integrate core observation, thin-section petrography, XRD analysis, thickness mapping, MICP, and μ-CT to characterize the lithofacies and pore structures of the Qixia Formation in the study area. Six lithofacies are recognized, including mudstone (F1), wackestone (F2), packstone (F3), grainstone (F4), rudstone (F5), and dolostone (F6), and F6 is further divided into three subtypes (F6-1, F6-2, F6-3). Dolostones exhibit superior reservoir quality relative to limestones, and among the dolostone, reservoir quality improves progressively from F6-1 to F6-3 with increasing crystal size and dolomite content. Dolostone distribution is spatially tied to E–W strike–slip faults, and its formation age coincides with documented fault activity, implicating these faults as the primary fluid conduits. Quantitative pore structure analyses further indicates that dolomitization enhanced permeability by enlarging pore–throat radii and improving macropore connectivity, with associated dissolution contributing additional secondary porosity.

Keywords: hydrothermal dolomitization; reservoir quality; pore structure; Permian Qixia Formation; Sichuan Basin

Check for updates

Academic Editor: Santanu Banerjee

Received: 7 January 2026
Revised: 25 February 2026
Accepted: 26 February 2026
Published: 28 February 2026

Copyright: © 2026 by the authors. Licensee MDPI, Basel, Switzerland. This article is an open access article distributed under the terms and conditions of the Creative Commons Attribution (CC BY) license.

1. Introduction

Dolostone reservoirs hold a critical position in the global oil and gas resource system, containing substantial hydrocarbon reserves [1,2]. The formation of dolostone reservoirs is a complex result controlled by the interplay of original depositional fabrics and dolomitization processes [3,4]. Previous studies on the formation mechanisms of porous dolostone reservoirs can be summarized into three main aspects: (1) Mole-per-mole replacement (dolomite replaces calcite) results in a theoretical porosity increase of 13% [5–7]; (2) dissolution accompanied by dolomitization leads to the creation new pore spaces in unreplaced calcite [8,9]; and (3) compaction reduces porosity with increasing burial depth [10], whereas

dolomitization improves the rock's resistance to compaction and thus helps preserve early pores [11–13]. Although these mechanisms are widely accepted, determining which process dominates in different geological settings and how to effectively predict the distribution of dolostone reservoirs remain fundamental challenges in current research.

Among various types of dolostone reservoirs, the structurally controlled hydrothermal dolostone (HTD) is one of the important exploration targets [14–18]. Its formation is closely related to the activity of hydrothermal fluids circulating along fault and fracture systems, generally resulting in substantial reservoir units [8,19,20]. This process is well-documented in classic models of fault-controlled and unconformity-controlled hydrothermal dolomitization, where fault zones and regional unconformities act as primary conduits for fluid migration, shaping the spatial pattern and geometry of dolostone bodies [21–23]. However, significant controversy remains regarding whether the impact of hydrothermal activity on reservoir quality is constructive or not. Some researchers proposed that hydrothermal fluids have the potential to generate dissolution pores [8,14,24]. In contrast, others argue that sustained input of fluids may also trigger extensive overdolomitization, which may destroy pore space [25,26]. This debate is clearly exemplified in the Qixia dolostone reservoirs of the Sichuan Basin. Although a hydrothermal origin has gradually gained consensus [27,28], the primary controlling factors governing the spatial distribution (whether dominated by sedimentary facies or faults) and their impact on reservoir quality (particularly pore structures) remain unresolved critical issues.

To directly resolve these specific controversies, this study integrates petrology, spatial statistical analysis of dolostone thickness relative to fault distance, and multi-scale quantitative pore structure analysis to investigate the characteristics and reservoir quality of the Qixia carbonates and to evaluate the impact of hydrothermal dolomitization on dolostone reservoir quality. Our work shifts the discussion from a qualitative debate on controlling factors to a multi-scale evaluation of reservoir consequence, offering a framework for the prediction of analogous hydrothermal dolostone reservoirs. This work provides key insights into regional dolostone controversies and global exploration of analogous hydrothermal dolostone reservoirs.

2. Geological Background

The Sichuan Basin (Figure 1a), located in the southwestern part of China, is a composite basin formed through multi-stages of tectonic movements built on a pre-Ediacaran crystalline basement [29–31]. From the Ediacaran to the Silurian, the Sichuan Basin was predominantly characterized by a marine depositional environment [29,30,32]. During the Ediacaran to the Early Cambrian, the regional tectonic setting gradually transitioned from extensional to compressional regimes [29,33]. From the late Early Cambrian to the Silurian, the basin experienced continuous northwestern compression, resulting in intense folding deformation and the development of several paleo-uplifts [30,34,35]. During the Devonian to Early Permian, the basin experienced unroofing, leading to the absence of the Devonian to Lower Permian strata within most of the basin [30,32]. The most intense denudation occurred in the northern part of the Central Sichuan Basin, where the Lower Cambrian strata are directly exposed [32]. By the Early to Late Permian, global sea-level rise resulted in marine deposition in the basin. During the depositional period of the Lower Permian Qixia Formation, the Sichuan Basin evolved into a carbonate platform environment [36–38]. In the late Middle Permian (approximately 260 Ma), the activity of the Emeishan Large Igneous Province (ELIP) triggered local extension and varying degrees of thermal anomalies in different regions within the basin [39–41]. By the Late Triassic, the eastward thrusting of the Songpan–Garze block along the western margin of the Sichuan Basin formed the Longmenshan Fault Zone (Figure 1a) [42–44].

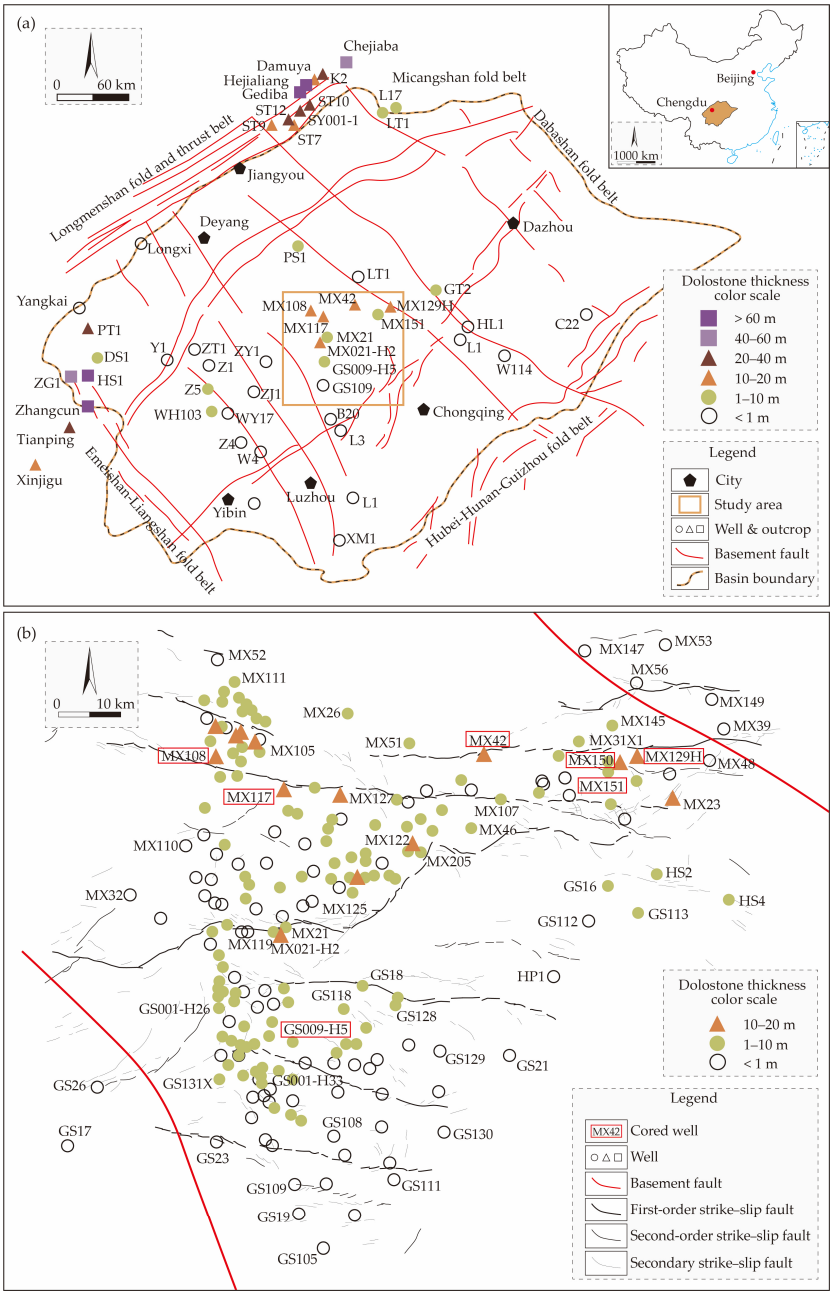

Figure 1. Location and geological context of the study area. (**a**) Regional setting within the Sichuan Basin, SW China, showing the locations of wells and sections, major basement fault systems (modified from Feng et al. [45]), and the distribution of dolostone thickness in the Permian Qixia Formation (modified from Huang et al. [36]; Li et al. [37]; Hu et al. [46]; Duan et al. [47]; Li et al. [48]; Tang et al. [49]); (**b**) regional setting within the study area, showing the locations of wells, the distribution of dolostone thicknesses in the Qixia Formation, major basement fault systems (modified from Feng et al. [45]), and strike–slip fault systems (modified from Guan et al. [50]; Ma et al. [51]).

Series of NE–SW and NW–SE trending basement faults [30] and multiple sets of strike–slip fault systems [50,52–55] developed in the Sichuan Basin (Figure 1a). The NE–SW trending faults formed during the Triassic and originated from the tectonic movements of the Longmenshan orogenic belt during the same period [30,33,56]. The NW–SE trending faults developed during the late Proterozoic and were reactivated from the Ediacaran to middle Permian [57,58]. In the Central Sichuan area, the Permian strata are crosscut by E–W-trending strike–slip faults [50,59,60]. These faults initially developed during the Devonian–Carboniferous period and were reactivated along certain segments by the end of

the Permian [43,61]. These faults initially developed during the Devonian–Carboniferous period and were reactivated along specific segments by the end of the Permian due to the Late Permian Emeishan rifting movement [43,61]. Based on vertical separation and lateral fault zone width, these faults are classified into first-order, second-order, and third-order strike–slip faults [50,59,60].

The study area is located in the Central Sichuan Basin (Figure 1a,b), with the Permian Qixia Formation as the stratigraphic interval of interest (Figure 2a). The Qixia Formation corresponds to the Cisuralian Series Kungurian Stage, based on a high-resolution biostratigraphic study (primarily based on conodonts, fusulinids, and radiolarians) [62]. In the study area, the Permian System is divided, in an ascending order, into the Liangshan, Qixia, Maokou, Longtan, and Changxing Formations [62,63]. The lowermost Liangshan Formation is characterized by bauxitic mudstone and carbonaceous mudstone [37] (Figure 2a). The lower part of the Qixia Formation is dominated by mudstone and bioclastic wackestone, and the upper part comprises grain-supported limestones [37] (Figure 2a).

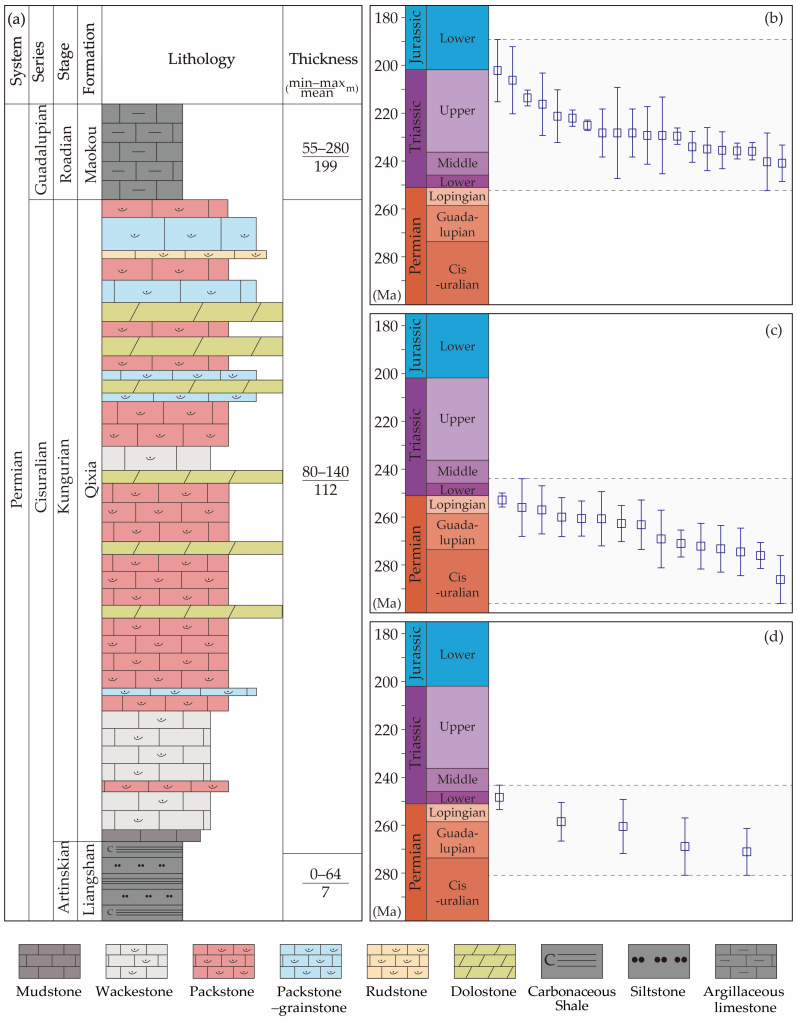

Figure 2. Lithostratigraphic column of the Permian Qixia Formation and compiled U-Pb dating results of dolomite from the formation across the basin. (**a**) Lithostratigraphic column of the Qixia Formation in the study area (data from Bai et al. [27]; He et al. [64]). (**b**) U-Pb ages of dolomite from the Qixia Formation in the Northwestern Sichuan Basin (data from Duan et al. [47]; Pan et al. [65]; Pan et al. [66]). (**c**) U-Pb ages of dolomite from the Qixia Formation in the study area (data from Bai et al. [27]; He et al. [67]; Lu et al. [68]; Zhu et al. [69]; Xiao et al. [70]). (**d**) U-Pb ages of dolomite from the Qixia Formation in the Northwestern Sichuan Basin (data from Xiao et al. [70]; Feng et al. [71]).

The dolostone of the Qixia Formation in the study area is an important hydrocarbon exploration target, but its distribution exhibits strong heterogeneity characterized by thin individual layers (0–4 m), vertically multi-layered (0–6 layers), and limited dolostone thickness (0–17.3 m) [46,72,73] (Figure 2a). The origin of the Qixia dolostone is still debatable, and several dolomitization models were proposed [27,64,74–76]. Recently, based on carbon and oxygen isotopic compositions, $^{87}Sr/^{86}Sr$ mass ratios, rare earth elemental concentrations, fluid inclusions, and dolomite U-Pb dating, the Qixia dolostone was classified as being of hydrothermal origin [27]. Basement faults that developed along the margins of the study area and/or the E–W-trending strike–slip faults (Figure 1b) were considered as the conduits for the hydrothermal dolomitizing fluids [42].

3. Materials and Methods

The research utilized a dense well network within the study area, consisting of over 200 wells with an average spacing of 2.5 km. This close spacing, with 52% and 82% of wells located within 2 km and 4 km of their nearest neighbor (Figure 1b), respectively, provides high-resolution spatial control. The dataset includes: (1) detailed observation, description, and sampling of 220 m of core from seven key wells (MX117, MX108, MX42, MX150, MX151, MX129H, GS009-H5); (2) cuttings from 12 additional wells; and (3) wireline logs from 225 wells.

A total of 234 core samples and 1082 cutting samples were used for making thin sections. Thin sections were ground to a standard thickness of 0.03 mm, with one third of each slide stained with Alizarin Red-S to distinguish dolomite from calcite [71]. Lithofacies identification of core and cuttings thin sections was conducted under polarized light microscopy following the classification schemes of Dunham [77] and Embry and Klovan [78]. To reveal more detailed petrographic features, cathodoluminescence (CL) microscopy was performed on 25 representative thin sections using a cold cathodoluminescence system (model CL8200 MK5, Cambridge Image Technology Ltd. CITL, Hertfordshire, Hertfordshire, UK) coupled with a polarizing microscope and a digital camera for image acquisition. For dolostones, crystal sizes were counted using ImageJ (version 1.54g) on 42 thin sections with 350 crystals per section, generating a total dataset of 14,700 data points. The classification of dolomite textures was according to established criteria by Sibley and Gregg [79]. Aiming to identify the pore types, a total of 42 core samples were prepared for cast thin sections with blue epoxy. The cast thin sections were ground to a standard thickness of 0.03 mm. Pore classifications were conducted under a polarizing microscope following the criteria established by Choquette and Pray [80].

Fifteen powdered samples were subjected to X-ray diffraction (XRD) to quantify relative mineral abundances. X-ray diffraction (XRD) analysis was performed at the State Key Laboratory of Oil and Gas Reservoir Geology and Exploitation, Southwest Petroleum University (Chengdu, China). Measurements were conducted on a Rigaku SmartLab SE diffractometer (Rigaku Corporation, Tokyo, Japan) operated at 40 kV and 40 mA with Cu-Kα radiation. The slit configuration included a 1° divergence slit, 1° scattering slit, and 3 mm receiving slit. Continuous scans were recorded from 5° to 45° 2θ with a step size of 0.02° and a scanning speed of 2°/min. Mineral identification and quantification of relative abundances were achieved through Rietveld refinement of the XRD patterns using Jade software (version 9.0.1) [81–85].

A total of 93 plug samples (2.5 cm in diameter and 5.0 cm in length) were drilled for conventional porosity and permeability measurements, consisting of 63 limestone samples (average sampling interval ~3 m) and 30 dolostone samples (average interval ~1 m). A note on sampling is warranted for the vuggy dolostone. To preserve plug integrity during coring and measurement, sampling deliberately avoided zones with the largest vugs, targeting

instead more consolidated, less vuggy representative areas. Consequently, the reported porosity and permeability for F6-3 may represent a lower bound for total reservoir capacity, as the contribution of larger vugs is not fully captured. This constraint has been considered in data interpretation. The measurements were conducted at the National Key Laboratory of Reservoir Geology and Development Engineering, Southwest Petroleum University (Chengdu, China), using an LGPM700 porosimeter–permeameter (Sanchez Technologies, Inc., FAR) with nitrogen as the injection medium. Measured porosity ranges from 0.1% to 60%, and permeability ranges from 0.00001 to 10 mD under a confining pressure of 70 MPa.

Ten plug samples (2.5 cm diameter × 5.0 cm length) were selected for mercury injection capillary pressure (MICP) analysis. These analyses were conducted at the School of Petroleum Engineering, Northeast Petroleum University (Daqing, China), utilizing a PoreMaster-60 high-pressure porosimeter (Quantachrome Instruments, Boynton Beach, FL, USA). All samples were washed with methanol and dried to a constant weight at 105 °C before mercury intrusion. The samples were then placed in a closed expansion instrument under vacuum. The mercury injection procedure implemented stepwise pressure increments up to 200 MPa and the process data was recorded. Pore–throat parameters were derived from the intrusion curves [86–88].

Eight plug samples (2.5 cm diameter × 5.0 cm height) and one full-diameter core sample (10 cm diameter × 10 cm height) were selected for micro-computed tomography (μ-CT) and pore structure characterization. The three-dimensional rock CT imaging was performed at the State Key Laboratory of Oil and Gas Reservoir Geology and Exploitation at Southwest Petroleum University (Chengdu, China). The core samples were scanned using a MicroXCT-400 three-dimensional reconstruction X-ray microscope manufactured by Xradia, Pleasanton, CA, USA. The voxel resolutions for the plugs and full-diameter core samples were 11.92 μm and 46.16 μm, respectively. Three-dimensional reconstruction and data processing were carried out using Avizo software (version 9.0.1) to calculate topological parameters, including equivalent pore radius, equivalent throat radius, pore volume, and coordination number [89–91]. During the processing of the μ-CT data, we applied a rigorous, size-based filter to all extracted pore and throat features. Specifically, only those structures with equivalent diameters exceeding twice the voxel resolution (i.e., >23.84 μm for plug samples) were included in the subsequent calculation of pore/throat size distributions and coordination numbers.

4. Results

4.1. Lithofacies

Based on the cores and thin-section observation and analysis, six lithofacies were identified: mudstone (F1), wackestone (F2), packstone (F3), packstone–grainstone (F4), rudstone (F5), and dolostone (F6). The dolostone (F6) is further subdivided into three subfacies: F6-1, F6-2, and F6-3. The characteristics and distribution of the lithofacies are shown in Table 1 and Figures 3–8.

Table 1. Lithofacies types and their characteristics.

Lithofacies		Stratigraphic Position and Physical Features	Textural Characteristics	Fossil Assemblage
F1	mudstone	Lower Qixia; grayish-black; tight	matrix-supported; <10% bioclast	mall-sized sponge spicules, non-fusulinid foraminifera
F2	wackestone	Lower Qixia; grayish-black; tight	matrix-supported;	echinoderm, non-fusulinid foraminifera, bryozoan debris.

Table 1. *Cont.*

Lithofacies		Stratigraphic Position and Physical Features	Textural Characteristics	Fossil Assemblage
F3	packstone	Middle to upper Qixia; dark gray; with small pores, moldic pore	grain-supported; 50–70% grain;	non-fusulinid foraminifera, echinoderm debris, ostracod fragments, gastropod fragments, fusulinids, calcareous algae, coral debris
F4	packstone –grainstone	Middle to upper Qixia; gray color; with small pores, moldic pore	grain-supported; 60–80% grain;	foraminifera, calcareous algae, coralloid algae, echinoderm debris, brachiopod fragments, ostracod valves, shell debris
F5	rudstone	Middle to upper Qixia; gray color; with small pores, moldic pore	grain-supported; 60–80% grain;	calcareous algae, bivalve fragments, ostracod valves, and shell debris
F6-1	dolostone	Middle to upper Qixia; gray color; with small pores, intercrystalline pores	fabric-destructive, planar-s	coralloid algae, echinoderm debris, fusulinids, and shell debris
F6-2	dolostone	Middle to upper Qixia; gray color; with small pores, vugs, intercrystalline pores	fabric-destructive, planar-s to nonplanar-a textures, crystal sizes 250–500 μm	coralloid algae, echinoderm debris, fusulinids, and shell debris
F6-3	dolostone	Middle to upper Qixia; gray color; with small pores, vugs, fractures, intercrystalline pores	fabric-destructive, planar-s to nonplanar-a textures, crystal sizes > 500 μm	\

4.1.1. Mudstone (F1)

This lithofacies exhibits a grayish-black color (Figure 3a). F1 appears matrix-supported, with the bioclast content less than 10%. The bioclasts mainly include small-sized sponge spicules and non-fusulinid foraminifera (Figure 4a). F1 is majorly distributed at the base of the Qixia Formation in the study area, with a cumulative thickness ranging from 5 m to 20 m (Figures 6 and 7).

4.1.2. Wackestone (F2)

This lithofacies displays a grayish-black color, with sparse bioclasts observed within the core (Figure 3b). F2 appears matrix-supported, and the main types of bioclasts include echinoderms, non-fusulinid foraminifera, and bryozoan debris. The bioclast contents range from 10% to 50% (Figure 4b), some of which are preferentially oriented parallel to bedding. F2 is majorly distributed at the base of the Qixia Formation, with a cumulative thickness ranging from 30 m to 40 m (Figures 6 and 7).

4.1.3. Packstone (F3)

This lithofacies displays a dark gray color, with abundant bioclasts observed within the core (Figure 3c). F3 appears grain-supported with grain content ranging from 50% to 70%, with intergranular spaces filled by carbonate mud (Figure 4c). The carbonate grains mainly comprise intraclasts and bioclasts. The intraclasts are sub-rounded-to-elliptical in shape, with diameters ranging from 50 μm to 300 μm. Bioclastic types include non-fusulinid foraminifera, echinoderm debris, ostracod fragments, gastropod fragments, *Fusulina*, calcareous algae, and coral debris, exhibiting long-axis dimensions between 200 μm and 500 μm. F3 is majorly distributed in the middle to upper parts of the Qixia Formation, with a cumulative thickness of 30 m to 50 m (Figures 6 and 7).

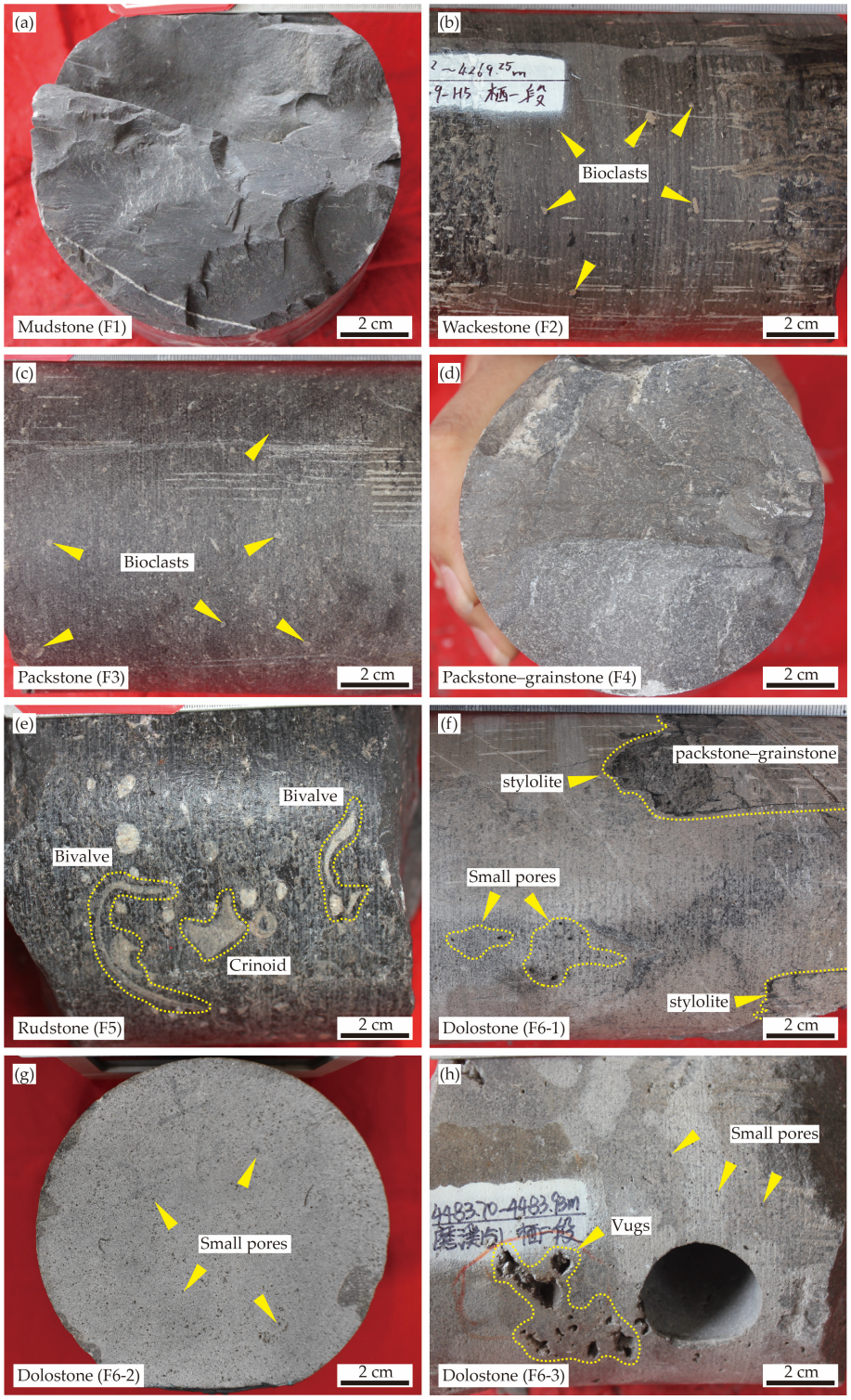

Figure 3. Core photographs showing: (**a**) mudstone (F1, Well MX151, 4524.28–4524.34 gray with a grayish-black color with minor bioclast fragments visible on the core surface; (**b**) wackestone (F2, Well GS009-H5, 4269.02–4269.25 m), with a grayish-black color and sparse bioclasts on the fracture surface; (**c**) packstone (F3, Well GS009-H5, 4271.92–4272.0 m), dark gray in color, displaying densely packed bioclasts; (**d**) packstone–grainstone (F4, Well GS009-H5, 4242.78–4242.94 m), gray in color, with abundant bioclast fragments on the core surface; (**e**) rudstone (F5, Well MX117, 4581.90–4581.98 m), gray in color, showing bivalve and crinoid; (**f**) dolostone (F6-1, Well GS009-H5, 4239.74–4239.91 m), medium to gray, small pores are observed on the core; (**g**) dolostone (F6-2, Well GS009-H5, 4240.20–4240.25 m), medium to gray, small pores are observed on the core; (**h**) dolostone (F6-3, Well MX151, 4483.70–4483.93 m), medium to gray, small pores and irregularly shaped vugs.

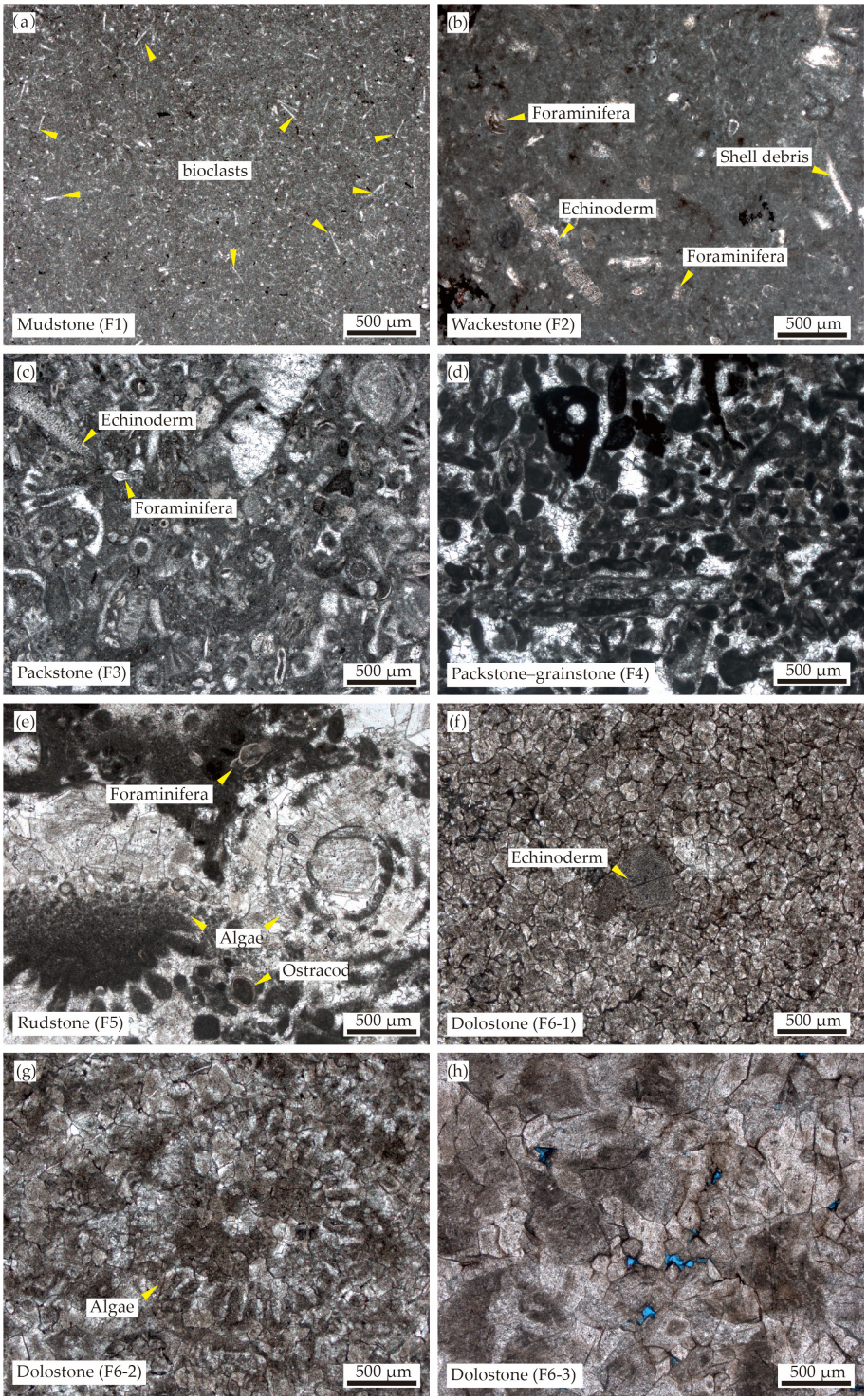

Figure 4. Photomicrographs showing characteristics of the identified lithofacies, all taken under plane-polarized light: (**a**) mudstone (F1, Well MX151, 4477.64 m), matrix-supported with sparse (<10%) sponge spicules; (**b**) wackestone (F2, Well MX129H, 4549.55 m), matrix-supported with echinoderms and non-fusulinid foraminifera; (**c**) packstone (F3, Well MX108, 4672.78 m), grain-supported with diverse bioclasts including foraminifera and echinoderm debris; (**d**) packstone–grainstone (F4, Well MX151, 4484.84 m), grain-supported with foraminifera and calcareous algae; (**e**) rudstone (F5, Well MX108, 4668.59 m), grain-supported with calcareous algae and bivalve fragments; (**f**) dolostone (F6-1, Well MX129H, 4519.38 m) with echinoderm debris ghost, showing planar-s to nonplanar-a textures; (**g**) dolostone (F6-2, Well MX108, 4671.10 m) with calcareous algae ghost, showing planar-s to nonplanar-a textures; (**h**) dolostone (F6-3, Well MX151, 4525.71 m) without apparent relict texture, showing planar-s to nonplanar-a textures.

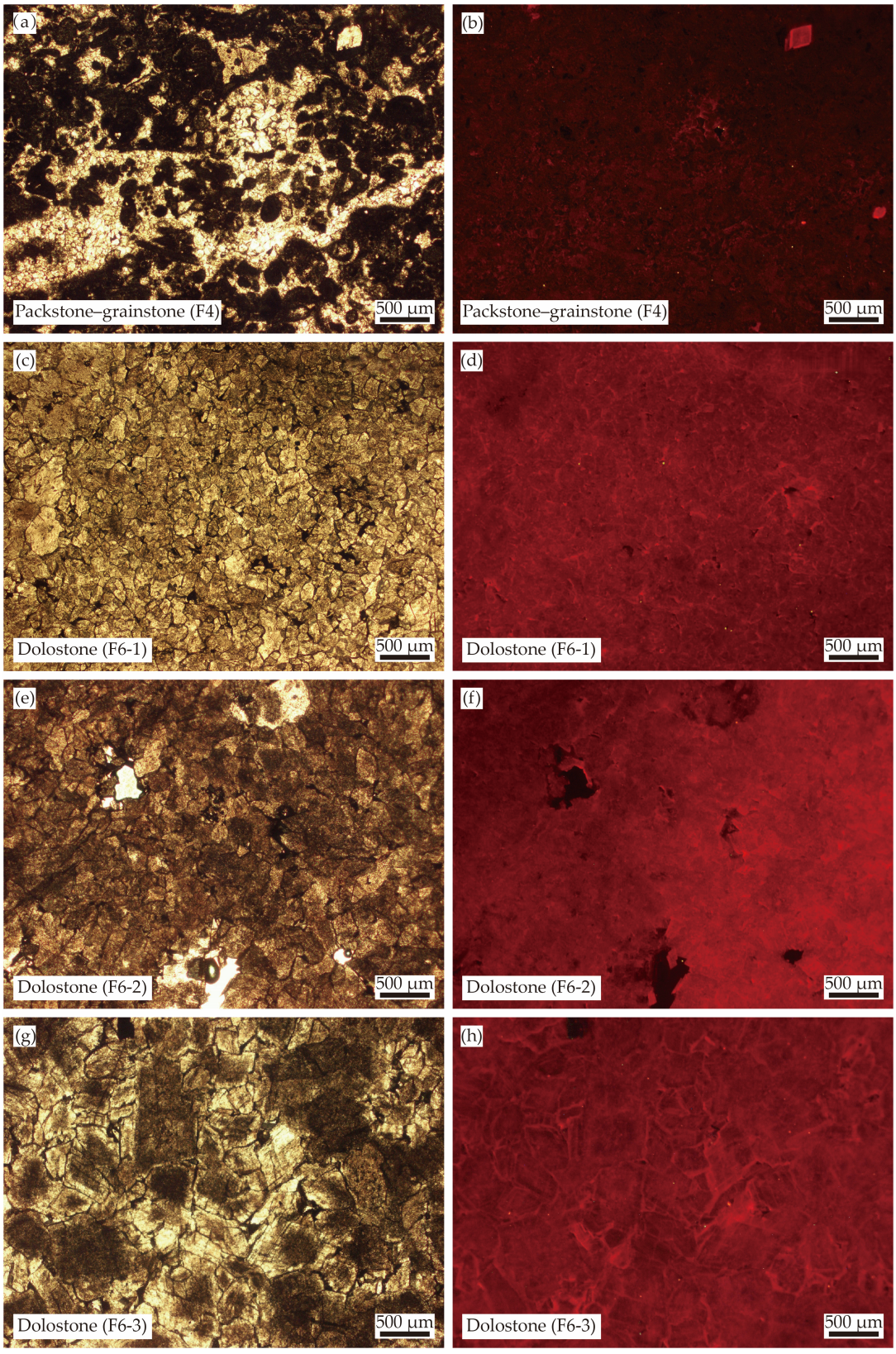

Figure 5. Photomicrograph pairs (plane-polarized light, PPL and cathodoluminescence, CL) showing characteristics of the identified lithofacies in the Qixia Formation: (**a**,**b**) packstone–grainstone (F4, Well MX117M 4604.10 m); (**c**,**d**) dolostone (F6-1, Well MX151, 4530.8 m); (**e**,**f**) dolostone (F6-2, Well GS009-H5, 4240.18 m); (**g**,**h**) dolostone (F6-3, Well GS009-H5, 4245.23 m).

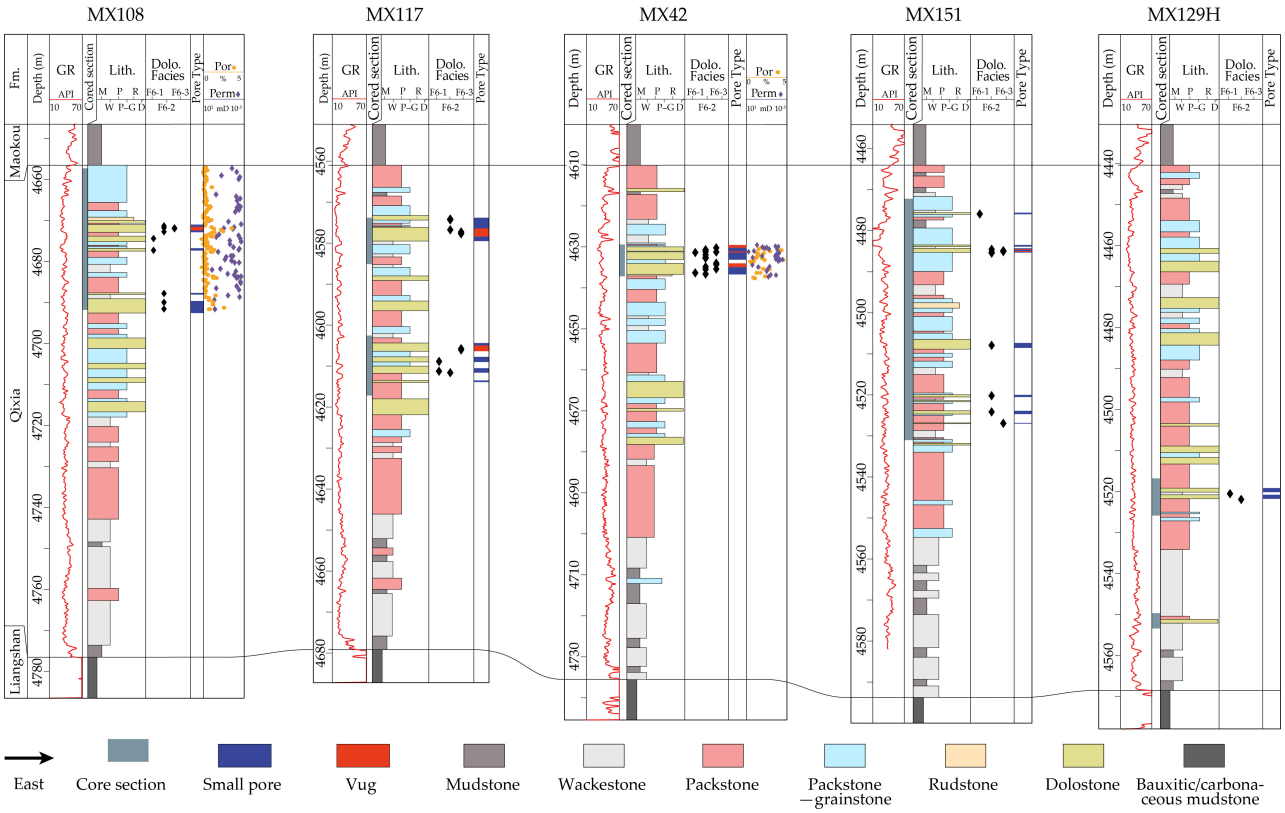

Figure 6. West–east stratigraphic well correlation of the Qixia Formation, showing the distribution of reservoir properties across the study area. The profile correlates gamma-ray (GR) log responses, cored intervals, lithofacies (Lith.), dolostone facies (Dolo. Facies), pore types, porosity (Por), and permeability (Perm).

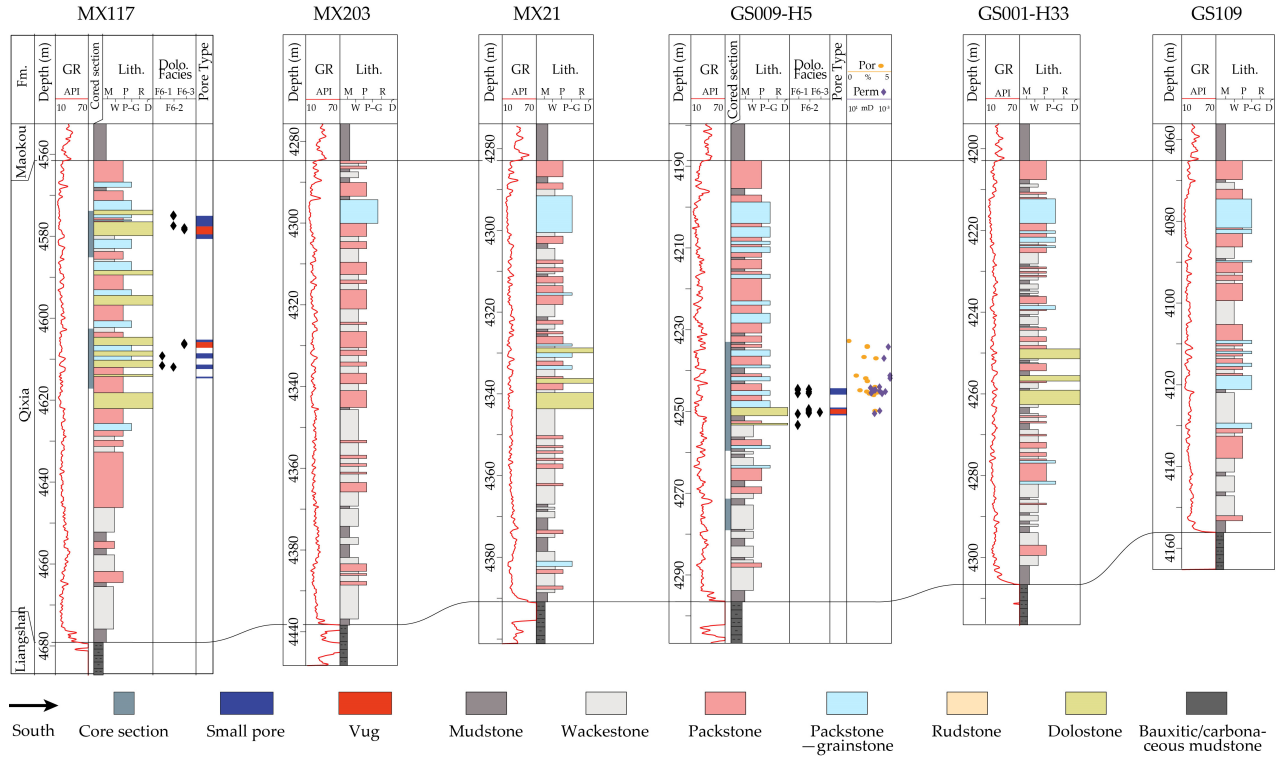

Figure 7. North–south stratigraphic well correlation of the Qixia Formation, showing the distribution of reservoir properties across the study area.

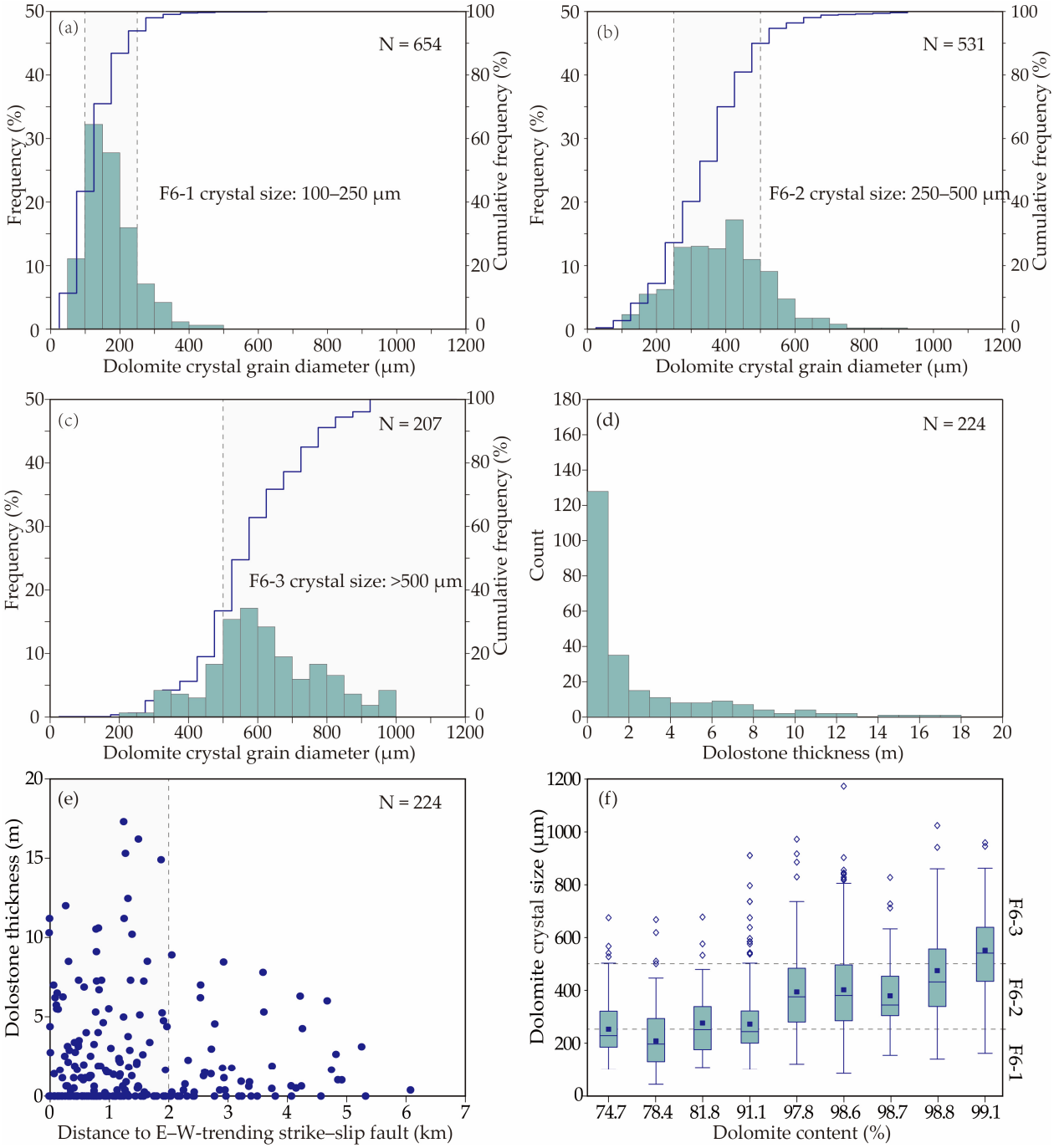

Figure 8. Characteristics of dolostones: (**a**–**c**) statistical plots showing crystal size distributions for samples F6-1, F6-2, and F6-3. Cyan bars: crystal frequency at each size interval; blue line: cumulative frequency; (**d**) histogram of dolostone thickness distribution from wells in the study area, showing that the vast majority of wells have dolostone thickness less than 2 m; (**e**) crossplots of dolostone thickness versus distance to the E–W-striking strike–slip fault; (**f**) box plots showing dolomite crystal size distribution across different dolomite content ranges. In (**f**): boxes, 25th–75th percentile (IQR); whiskers, range within 1.5 IQR; horizontal line, median; solid square, mean.

4.1.4. Packstone–Grainstone (F4)

This lithofacies displays a gray color (Figure 3d). F4 appears grain-supported, with grain content ranging from approximately 60% to 80%, with intergranular spaces filled by sparry cements and carbonate mud (Figure 4d). Under cathodoluminescence, F4 exhibits a very dull red luminescence, with bioclasts and sparry calcite cements showing closely

similar luminescence (Figure 5a,b). The carbonate grains principally comprise bioclasts. Bioclasts are primarily composed of foraminifera, calcareous algae, coralloid algae, echinoderm debris, brachiopod fragments, ostracod valves, and shell debris, exhibiting long-axis lengths between 300 μm and 500 μm. F4 is primarily distributed in the middle to upper parts of the Qixia Formation in the study area, with a cumulative thickness of 10 m to 20 m (Figures 6 and 7).

4.1.5. Rudstone (F5)

This lithofacies displays a gray color, with abundant bioclasts observed within the core (Figure 3e). The long-axis lengths of bioclasts predominantly range from 0.2 mm to 5 mm (Figure 3e). It appears grain-supported, with grain content ranging from approximately 60% to 80%, of which grains larger than 2 mm constitute approximately 50% (Figure 4e). The intergranular spaces are predominately filled by sparry cements, and partly filled by carbonate mud (Figure 4e). The carbonate grains principally comprise bioclasts, including calcareous algae, bivalve fragments, ostracod valves, and shell debris (Figure 4e). F5 is primarily distributed in the middle to upper parts of the Qixia Formation, with the thickness generally less than 1 m (Figures 6 and 7).

4.1.6. Dolostone (F6)

This lithofacies exhibits a medium gray to light gray color (Figure 3f–h). The dolostone in the Qixia Formation is generally fabric-destructive, and comprises dolomite crystals with sizes ranging from 100 to 800 μm (Figure 4f–h). They are subdivided into three groups: F6-1 (Figures 3f and 4f), F6-2 (Figure 4g), and F6-3 (Figure 4h). In cathodoluminescence, all three subtypes of dolostone display a dark red luminescence, with F6-1 and F6-2 displaying a slightly brighter intensity compared to F6-3 (Figure 5c–h). F6-1 majorly comprises planar-s dolomites with crystal sizes of 100–250 μm (>50%, Figures 4f and 8a), and F6-2 comprises planar-s dolomites with crystal sizes of 250–500 μm (>50%, Figures 4g and 8b). Locally, some bioclasts are partly preserved in F6-1 and F6-2, including coralloid algae, echinoderm debris, fusulinids, and shell debris (Figure 4f,g). The dolomite crystals in F6-3 show planar-s to nonplanar-a textures with crystal sizes principally larger than 500 μm (Figures 4h and 8c).

The dolostones (F6-1 to F6-3) are predominantly developed within the middle–upper Qixia Formation as thin layers (0–4 m) (Figures 6 and 7), and their cumulative thickness per well exhibits high heterogeneity, ranging from 0 to 17.3 m (mean ± standard deviation: 2.2 ± 3.3 m) (Figures 6, 7 and 8d, and Table A1). The thickness distribution shows a strong spatial correlation with the E–W-trending strike–slip fault system. Among the 225 wells penetrating the formation, all 10 wells intersecting dolostone thicker than 10 m are located within 2 km of these faults, and 39 of the 41 wells (95.1%) with thickness exceeding 5 m lay within a 4 km corridor (Figure 8e, and Table A1). Notably, while not every proximal well encountered thick dolostone, all significant accumulations (>5 m) are confined to these fault-proximal zones. This observation demonstrates a correlation between dolostone thickness/distribution and the faults.

4.2. Mineral Composition

The analyzed limestone and dolostone samples show dolomite contents ranging from 0 to 99.6% (Table 2). In dolostones (dolomite contents > 50%), dolomite crystal size increases progressively with higher dolomite content (Figure 8f). The predominant crystal size (defined as the interquartile range, 25th–75th percentile) for specific intervals are 100–350 μm (dolomite content: 70–90%), 200–500 μm (dolomite content: 90–99%), and 350–650 μm (dolomite content: >99%).

Table 2. Mineral composition of carbonate rocks from the Qixia Formation in the study area.

No.	Wells	Depth (m)	Mineral Content (%)					
			Dolomite	Calcite	Quartz	Clay Minerals	Plagioclase	Pyrite
1	MX42	4659.63	2.8	96.4	0.3	0.4	0	0
2	MX42	4654.75	3.9	95.4	0.2	0.4	0	0
3	MX42	4649.47	28.5	70.7	0.4	0.4	0	0
4	MX42	4652.46	74.7	24.3	0.3	0.2	0.4	0
5	MX42	4650.39	81.8	17.9	0.1	0.2	0	0
6	MX42	4657.27	97.8	1.8	0	0.1	0.3	0
7	MX42	4651.5	98.8	0.7	0.1	0.1	0.3	0
8	MX150	4482.98	1.1	51.0	47.1	0.3	0	0.4
9	GS009-H5	4331.61	0	99.3	0.2	0.5	0	0
10	GS009-H5	4239.75	20.3	78.7	0.5	0.4	0	0
11	GS009-H5	4244.86	78.4	21.3	0.1	0.2	0	0
12	GS009-H5	4245.45	91.1	8.4	0	0.1	0.4	0
13	GS009-H5	4245.13	98.6	1.0	0	0.1	0.3	0
14	GS009-H5	4240.15	98.7	0.5	0.2	0.1	0.5	0
15	GS009-H5	4240.38	99.1	0.5	0	0.1	0.3	0

4.3. Pore Types and Structures

4.3.1. Pore Types

Based on the observation of cores, the pore types include small pores (Figure 9a), vugs (Figure 9b), and fractures (Figure 9c). The small pores, with sizes less than 2 mm, are generally distributed in packstone–grainstone (F4) and dolostones (F6-1 to F6-3). The vugs are exclusively developed in F6-3, with diameters ranging from 2 to 10 mm, and they generally show rounded to sub-rounded shapes (Figure 9b). The fractures are also observed in F6-2 and F6-3, with widths ranging from 0.3 to 2 cm, and they are partly filled by dolomite and calcite cements (Figure 9c).

Thin sections were used to characterize the microscopic features of small pores. The small pores correspond to either moldic pores within the limestones (F4) (Figure 9d,e) or intercrystalline pores within the dolostones (F6-1 to F6-3) (Figure 9a,b,f–i). The moldic pores are commonly located in bioclasts with micrite envelop, and some of them are filled by bitumen (Figure 9d,e). Intercrystalline pores occur in F6-1, F6-2, and F6-3, exhibiting distinct size distributions. In F6-1, the diameters of intercrystalline pores mainly group between 50 and 100 μm (Figure 9f). In F6-2, the diameters are primarily in the range of 50 to 500 μm (Figure 9g), with some pores reaching up to 1500 μm. In F6-3, the diameters of intercrystalline pores mainly occur between 50 and 1000 μm (Figure 9h,i).

4.3.2. Porosity and Permeability

The porosities of analyzed limestone (F1, F2, F3, F4, F5) and dolostone (F6) samples range from 0.1 to 9.4% (2.6 ± 2.1%, n = 93), and the permeabilities range from 0.00002 mD to 3.15 mD (0.178 ± 0.59 mD, n = 93) (Figure 10a,b and Table A2). The porosity and permeability of limestone are 0.1–9.4% (2.6% ± 2.1%, n = 93) (n = 63) and 0.00002–3.15 mD (0.08 ± 0.42 mD) (n = 63), respectively, which are significantly lower than those of dolostone with a porosity of 2.2–9.4% (4.2% ± 2.0%) (n = 30) and a permeability of 0.0008–2.81 mD (0.38 ± 0.84 mD) (n = 30) (Figure 10c,d). F6-1, F6-2, and F6-3 show porosities of 2.5–3.9% (3.2 ± 0.7%) (n = 2), 2.2–9.4% (3.9 ± 1.9%) (n = 16), and 2.3–9.2% (4.7 ± 2.2%) (n = 12), and permeabilities of 0.002–2.80 mD (0.08 ± 0.13 mD) (n = 2), 0.0008–0.48 mD (0.06 ± 0.12 mD) (n = 16), and 0.002–2.78 mD (0.62 ± 1.03 mD) (n = 12), respectively (Figures 10e and 9f).

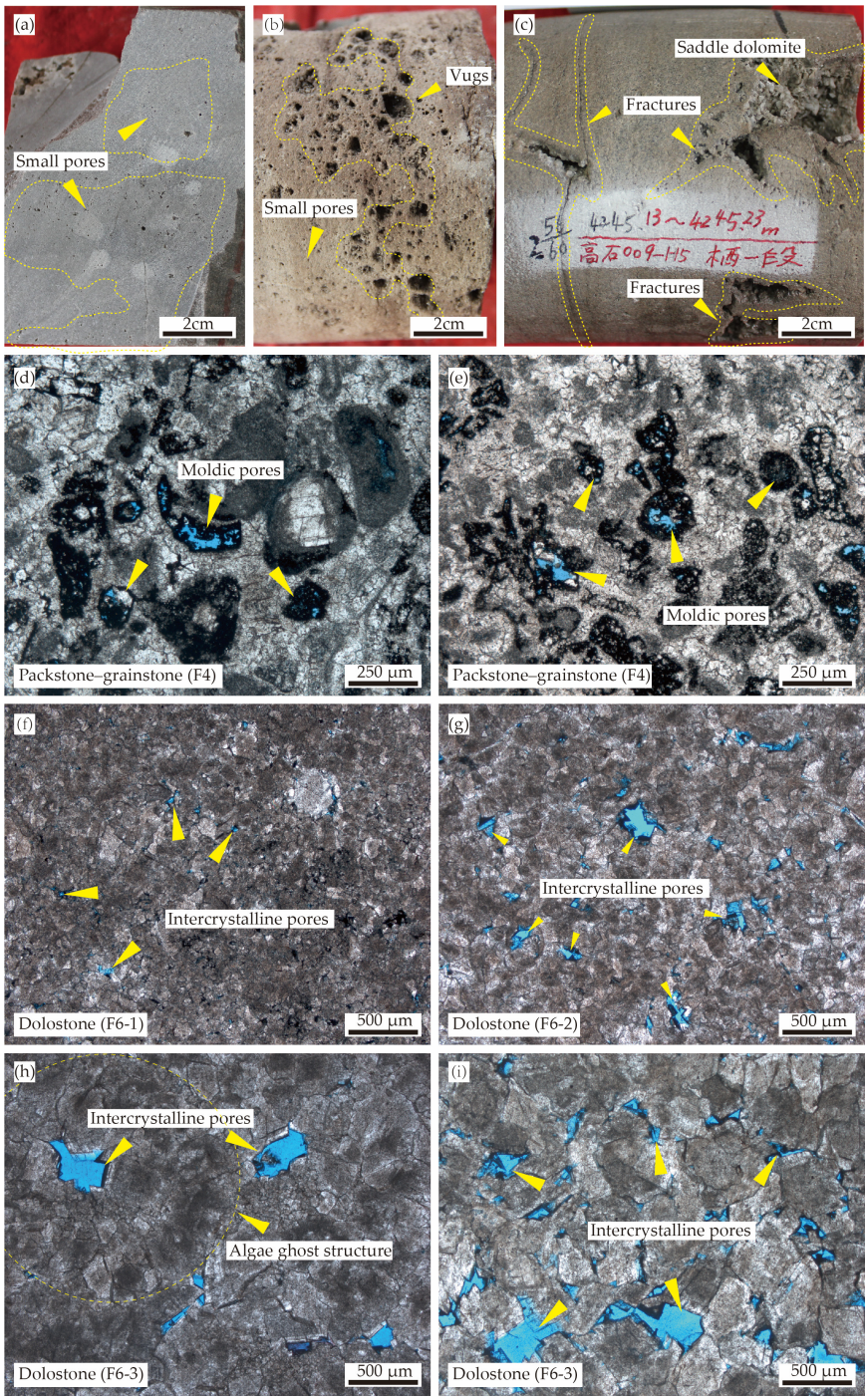

Figure 9. Core photographs and plane-polarized light micrographs of resin-impregnated thin sections illustrating pore types in the Qixia Formation, Central Sichuan Basin: (**a**) small pores (Well MX117, 4574.22–4574.29 m, F1), the pore sizes are less than 2 mm; (**b**) vugs and small pores (Well MX150, 4501.82–4501.89 m, F6-3), the vugs show rounded to sub-rounded shape with diameters ranging from 2 to 10 mm; (**c**) fractures (Well GS009-H5, 4245.13–4245.23 m, F6-3), with widths of 0.2–3 cm, partially filled by dolomite cement; (**d**) moldic pores (Well MX42, 4650.11 m, F4), with pore sizes of 50–250 μm, that are partially or completely filled by bitumen ranging from complete to partial; (**e**) moldic pores (Well MX42, 4650.25 m, F4), with pore sizes of 50–200 μm, that are partially or completely filled by bitumen ranging from complete to partial; (**f**) intercrystalline pores (MX151, 4484.5 m, F6-1), with diameters of 50–100 μm, some of which are completely filled by bitumen; (**g**) intercrystalline pores (MX42, 4651.7 m, F6-3), with diameters of 50–500 μm; (**h**) intercrystalline pores and algae ghost structure (MX150,4499.7 m, F6-2), with a maximum pore diameter of 1200 μm; (**i**) intercrystalline pores (MX150, 4502.4 m, F6-3), with diameters of 50–700 μm.

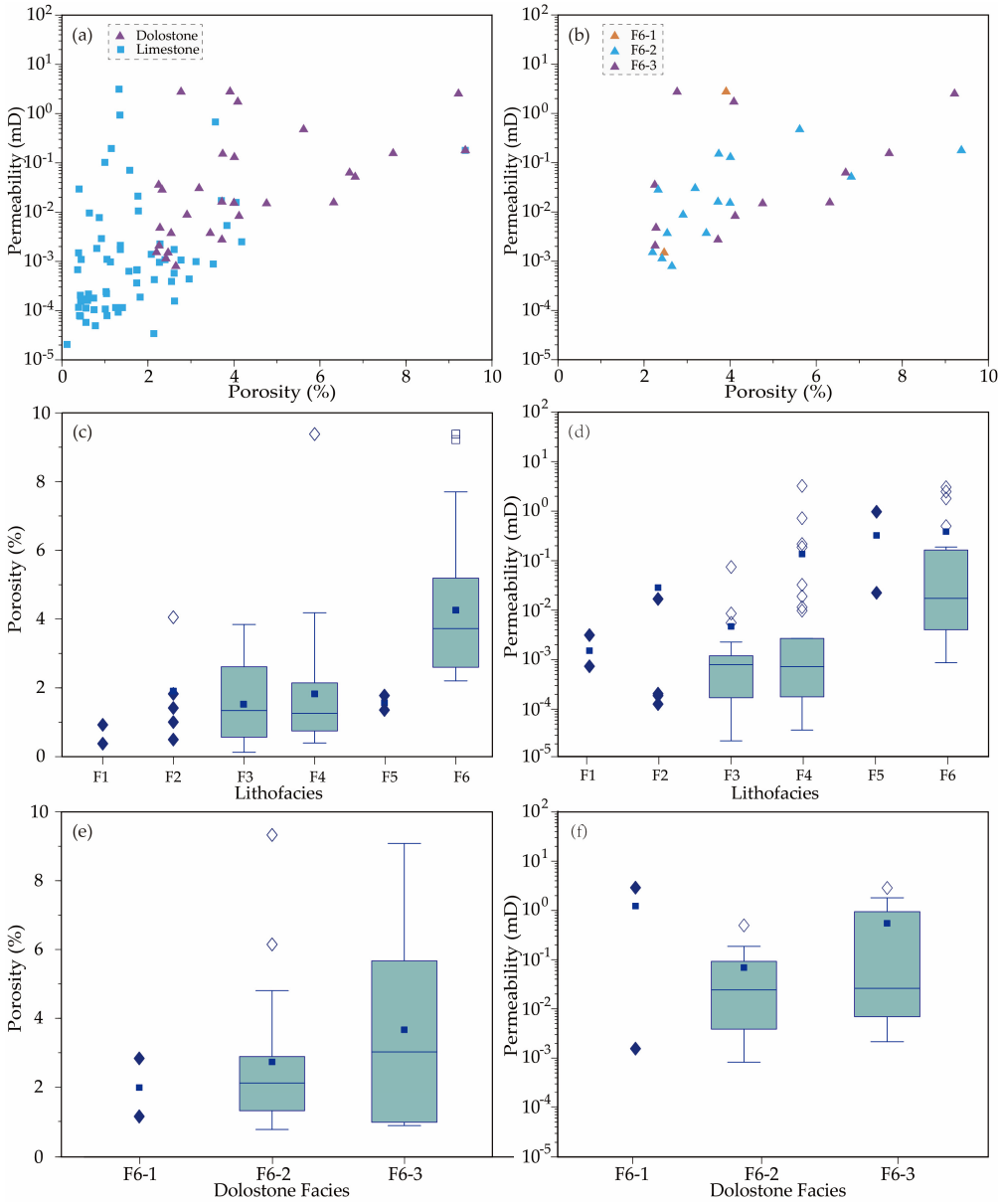

Figure 10. Petrophysical characteristics of diverse lithofacies in the Qixia Formation, Central Sichuan Basin: (**a**) porosity–permeability scatter plots of dolostone and limestone; (**b**) porosity–permeability scatter plots of dolostones (F6-1, F6-2, and F6-3); (**c**,**d**) porosity and permeability scatter plots of carbonate rocks from different lithofacies. Overall, both porosity and permeability of limestone are lower than those of dolostone; (**e**,**f**) porosity and permeability scatter plots of dolostones from different sub-lithofacies. In (**c**–**f**): boxes, 25th–75th percentile (IQR); whiskers, range within 1.5 IQR; horizontal line, median; solid square, mean; hollow diamonds, outliers.

4.3.3. MICP

The MICP analyses show that the pore structures of F3, F4, and F6-1 are similar, characterized by small and well-sorted pore–throats (Figure 11a,b). The displacement pressures (P_{cd}) range from 2.7 MPa to 13.8 MPa (7.2 ± 3.7 MPa, n = 5), and the maximum mercury saturation (S_{max}) obtained for individual samples ranges from 37.1% to 69.3% (57.1 ± 10.9%, n = 5). The calculated maximum pore–throat radii (R_a) and radii of median distribution (R_{50}) are 0.05–0.27 μm (0.1 ± 0.1 μm, n = 5) and 0.01–0.04 μm (0.02 ± 0.01 μm, n = 5), respectively. The sorting coefficients (S_p) range from 1.3 to 2.6 (2.0 ± 0.4, n = 5) (Table 3). The pore–throat radii distribution curves show bimodal peaks at 0.03–0.08 μm and 0.1–0.3 μm (Figure 12a,b).

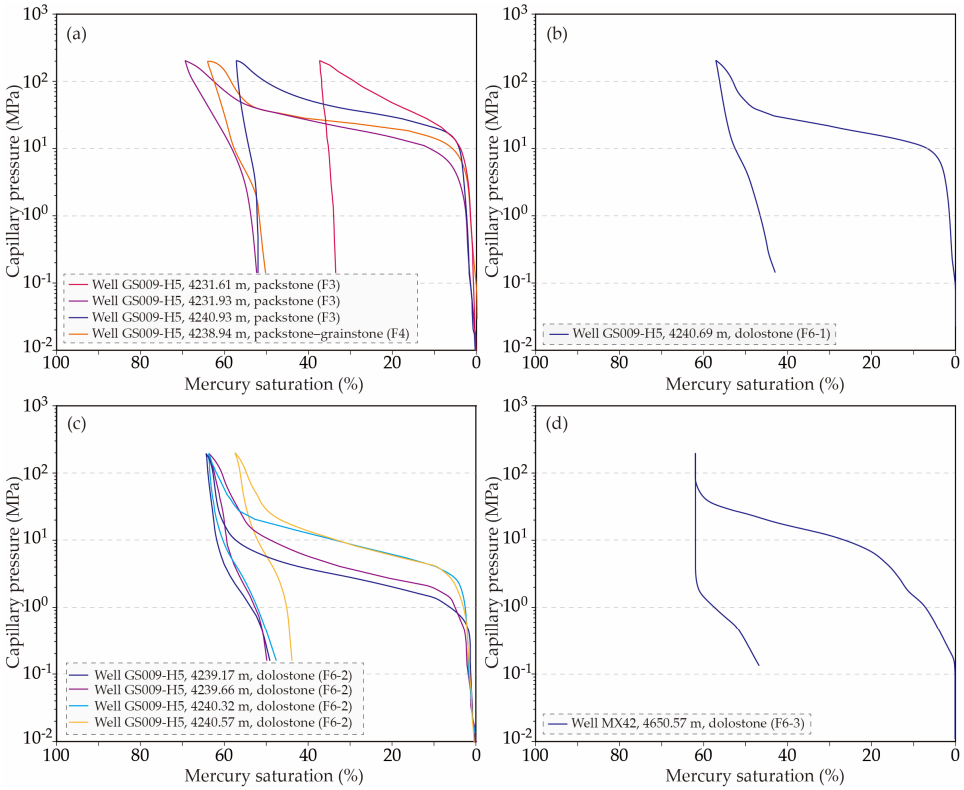

Figure 11. MICP curves for (**a**) packstone (F3) and packstone–grainstone (F4), (**b**) F6-1, (**c**) F6-2, and (**d**) F6-3.

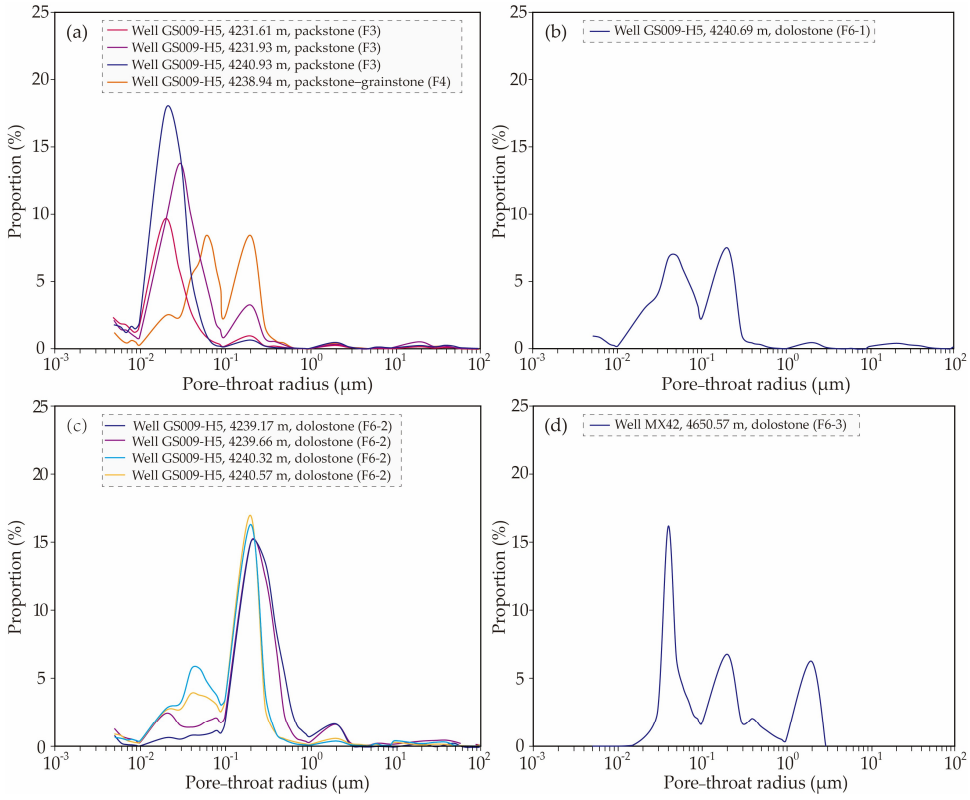

Figure 12. Pore–throat radius distribution of different lithofacies in the Qixia carbonate, based on high-pressure mercury injection data. Subplots a to d, respectively, display the pore–throat radius distribution characteristics of: packstone and packstone–grainstone (**a**), F6-1 (**b**), F6-2 (**c**), and F6-3 (**d**).

Table 3. Pore structure parameters of different lithofacies in the Qixia Formation carbonates in the study area (data from high-pressure mercury injection).

No.	Well	Depth (m)	Lith.	Por (%)	Perm (mD)	Entry Pressure (M_{pa})	Pore–Throat Radius (μm)		Sorting Coefficient	Skewness	Homogeneity Coefficient	Hg Saturation	
				φ	K	P_{cd}	R_a	R_{50}	S_p	S_{kp}	α	S_{max}	S_r
1	GS009-H5	4231.61	F3	2.2	0.00	8.3	0.09	/	2.2	−0.3	0.2	37.1	33.2
2	GS009-H5	4231.93	F3	3.8	0.01	5.5	0.13	0.02	2.0	−0.2	0.2	69.3	52.2
3	GS009-H5	4240.93	F3	3.5	0.00	13.8	0.05	0.01	2.1	−0.3	0.3	57.0	51.8
4	GS009-H5	4238.94	F4	3.7	0.02	2.7	0.27	0.04	1.3	0.2	0.2	64.0	50.1
5	GS009-H5	4240.69	F6-1	3.9	2.81	5.5	0.13	0.02	2.6	−0.4	0.3	57.9	43.7
6	GS009-H5	4239.17	F6-2	9.4	0.18	0.7	1.09	0.13	1.4	0.2	0.2	64.5	49.2
7	GS009-H5	4239.66	F6-2	6.8	0.05	0.5	1.57	0.07	2.1	0.2	0.1	63.9	50.0
8	GS009-H5	4240.32	F6-2	4.0	0.13	2.7	0.27	0.04	1.3	0.2	0.3	63.9	47.8
9	GS009-H5	4240.48	F6-2	2.9	0.01	2.7	0.27	0.03	1.7	0.1	0.3	57.4	44.0
10	MX42	4650.57	F6-3	7.7	0.16	0.2	14.38	0.03	4.1	1.4	\	61.9	46.6

Note: Lith. = lithofacies, Por = porosity, Perm = permeability.

Relative to F6-1, F6-2 exhibits larger pore–throat sizes (Figure 11c). The P_{cd} values of F6-2 range from 0.5 to 2.8 MPa (1.7 ± 0.6 MPa, n = 4), and the S_{max} values have a range of 57.4–64.5% (62 ± 2.9%, n = 4). The calculated R_a and R_{50} values range from 0.3 μm to 1.6 μm (0.80 ± 0.56 μm, n = 4) and 0.03 to 0.1 μm (0.06 ± 0.04 μm, n = 4), respectively. The sorting coefficients range from 1.3 to 2.1 (1.6 ± 0.3, n = 4) (Table 3). The pore–throat radii distribution curves show bimodal peaks at 0.1–0.7 μm and 0.02–0.1 μm (Figure 12c). F6-3 is characterized by the largest pore–throat sizes and the worst sorting (Figure 11d). The MICP analyses of F6-3 show that the P_{cd} value is 0.2 MPa (n = 1), and the S_{max} value is 61.9% (n = 1). The calculated R_a and radius of R_{50} values are 4.4 μm (n = 1) and 0.03 μm (n = 1), respectively. The sorting coefficient is 4.1 (n = 1) (Table 3). The pore–throat radius focusses on three intervals, i.e., 0.02–0.1 μm, 0.1–0.7 μm, and 1–2 μm (Figure 12d).

4.3.4. Micro-Computed Tomography Scanning (μ-CT)

The micro-computed tomography scanning (μ-CT) also shows significant differences in the pore size distribution of distinct lithofacies (Figures 13 and 14, and Table 4). The pore sizes in F3, F4, and F6-1 concentrate in the range of 10–200 μm (98.0% to 98.8% in number and 89.7% to 93.4% in volume, n = 854) (Figure 14a,b). F6-2 and F6-3 exhibit a broad pore size distribution. This is characterized by a disconnection between pore number and volume: smaller pores dominate numerically, while larger pores dominate volumetrically. In terms of number, most pores fall within the 10–100 μm range (F6-2: 89.3%, F6-3: 86.9%), while, in terms of volume, pores measuring 200–2000 μm account for the largest proportion of F6-2 (4.2% in number while 75.9% in volume, n = 165), and pores measuring 1000–10,000 μm account for the largest proportion of F6-3 (0.2% in number while 92.9% in volume, n = 864) (Figure 14c,d).

The pore–throat coordination numbers vary significantly across lithofacies and exhibit correlations with pore radius dimensions. Accurate measurements of throat radius distribution curves and pore–throat coordination number of F3, F4, and F6-1 dolostone are unattainable in the acquired CT dataset due to its limited resolution. In F6-2, the equivalent throat radii are primarily concentrated within the range of 30–100 μm (Figure 14e), and the coordination numbers are in the range of 1–7 (2.6 ± 1.8, n = 89) (Figure 14f). Equivalent radius-specific analysis reveals coordination numbers of 1–2 (1.3 ± 0.5, n = 15), 1–7 (2.5 ± 1.6, n = 70), and 3–7 (5.5 ± 1.5, n = 8) for pores within 10–100 μm, 100–1000 μm, and larger than 1000 μm ranges, respectively (Figure 14f). In F6-3, the equivalent throat radii are primarily concentrated within the range of 100–200 μm (Figure 14g), the coordination numbers are in the range of 1–14 (2.6 ± 2.4, n = 217) (Figure 13h), and they are in the ranges of 1–3 (1.3 ± 0.6, n = 77), 1–8 (2.5 ± 1.6, n = 102), 1–15 (4.9 ± 3.9, n = 28), and

2–13 (6.5 ± 2.9, n = 10) for pores within the 0–100 µm, 100–1000 µm, 1000–10,000 µm, and 10,000–100,000 ranges, respectively (Figure 14h).

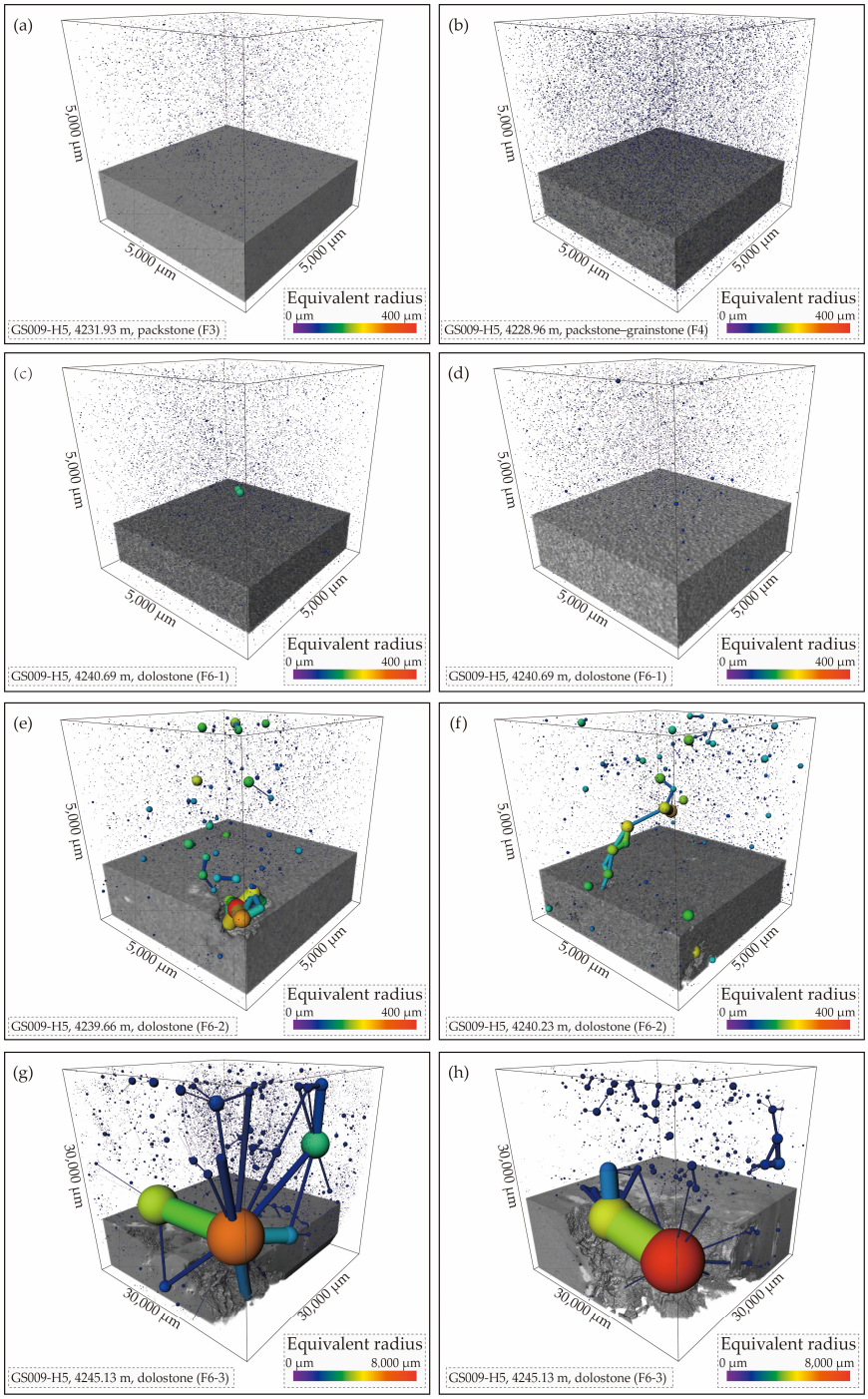

Figure 13. Pore-network model of the Qixia Formation carbonate rocks. This 3D visualization, derived from a sub-volume of the full-field CT scan, uses spheres and cylinders to represent pores and throats (scaled by factors of 0.5 and 0.35, respectively). (**a**) Packstone (F3, Well GS009-H5, 4231.93 m) with isolated pores. (**b**) Packstone–grainstone (F4, Well GS009-H5, 4228.96 m) with isolated pores. (**c**,**d**) Dolostone (F6-1, Well GS009-H5, 4240.69 m) featuring small pores and poor connectivity. (**e**) Dolostone (F6-2, Well GS009-H5, 4239.66 m) with well-connected small pores. (**f**) Dolostone (F6-2, Well GS009-H5, 4240.23 m) containing small pores and local fractures that form a highly connected system. (**g**,**h**) Dolostone (F6-3, Well GS009-H5, 4245.13–4245.23 m) characterized by relatively large pores, good connectivity, and a high pore–throat coordination number (averaging up to 9).

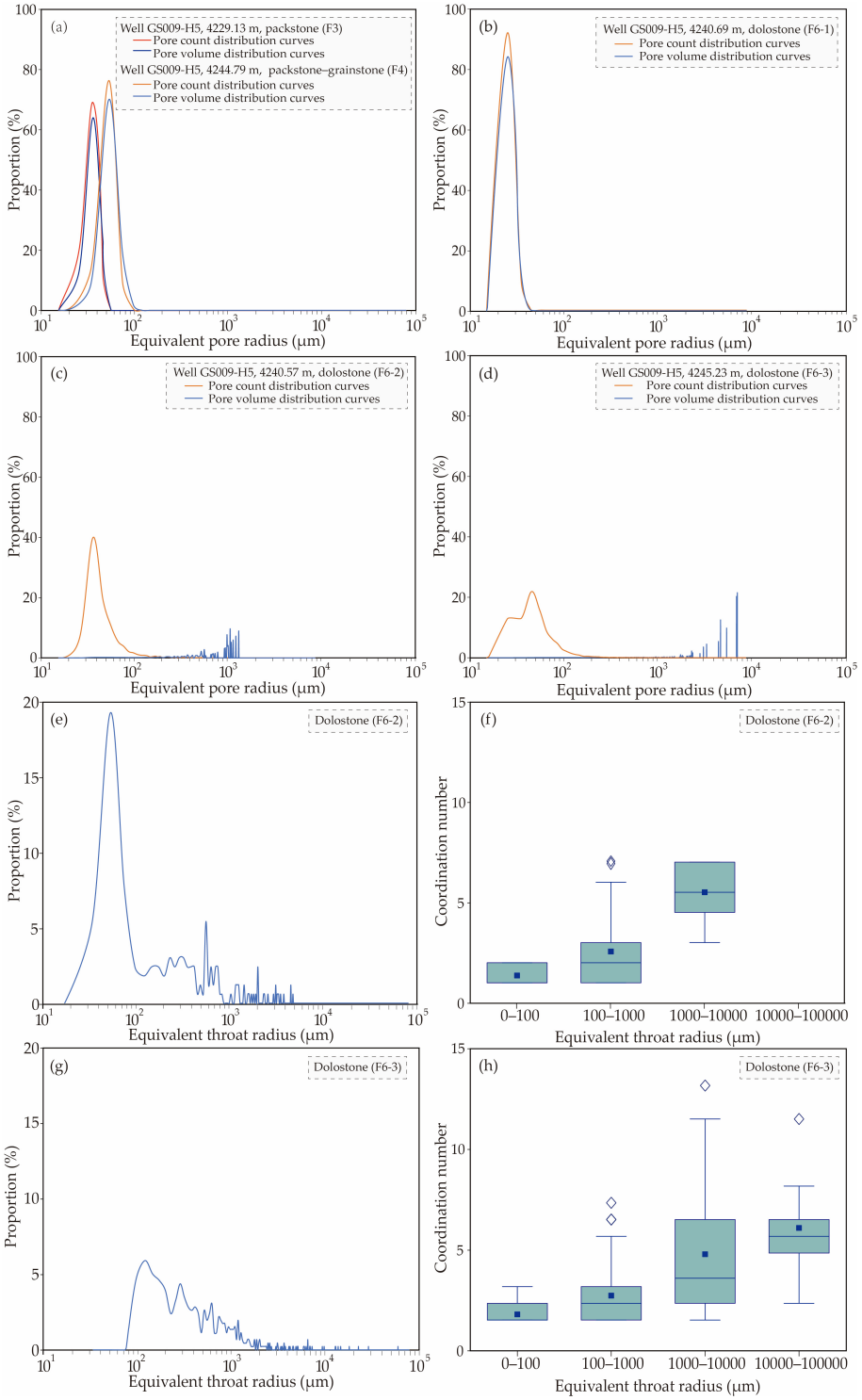

Figure 14. Pore structure characteristics of the Qixia Formation carbonate rocks in the study area. All data was derived from CT volume processing: (**a**–**d**) pore size number and pore volume distribution curves for the F3/F4, F6-1, F6-2, and F6-3; (**e**) throat equivalent radius distribution curves for F6-2; (**f**) box plots of pore–throat coordination number for different equivalent pore radius for F6-2 (n = 89); (**g**) throat equivalent radius distribution curves for F6-3; (**h**) box plots of pore–throat coordination number for different equivalent pore radius for F6-3 (n = 217). In (**f**,**h**): boxes, 25th–75th percentile (IQR); whiskers, range within 1.5 IQR; horizontal line, median; solid square, mean; hollow diamonds, outliers.

Table 4. Proportions of number and volume of pores with different equivalent radius of the Qixia Formation carbonates in the study area (data from μ-CT).

No.	Well	Depth (m)	Lithofacies	Pore Equivalent Radius and Its Proportion by Number/by Volume		
				10–100 (μm)	100–1000 (μm)	1000–10,000
1	GS009-H5	4231.93–4232.00	F3	99.9%/99.9%	0.1%/0.1%	0%/0%
2	GS009-H5	4240.93–4241.07	F3	99.8%/99.9%	0.2%/0.1%	0%/0%
3	GS009-H5	4228.96–4229.05	F4	99.2%/99.7%	0.8%/0.3%	0%/0%
4	GS009-H5	4238.94–4239.06	F4	99.1/98.9%	0.8%/1%	0.1%/0.1%
5	GS009-H5	4240.69–4240.75	F6-1	97.9%/97.6%	2.0%/2.3%	0.1%/0.1%
6	GS009-H5	4239.66–4239.72	F6-2	87.7%/6.3%	10.6%/35.8%	1.7%/57.9%
7	GS009-H5	4240.32–4240.38	F6-2	89.9%/1.2%	9.8%/46.2%	0.3%/52.6%
8	GS009-H5	4245.13–4245.23	F6-3	86.9%/0.3%	12.9%/6.8%	0.2%/92.9%

5. Discussion

5.1. What Controls the Distribution of the Qixia Dolostone?

Previous studies have focused on the formation time and fluid mechanism of the Qixia dolostone [27,92–94]. The reported dolomite U-Pb dating indicates that the hydrothermal dolostone in the study area formed at 286.0–252.9 Ma (Figure 2c) [27,67–70], and its comparable geochemical signature [27,73] suggests the three dolostone types (F6-1, F6-2, and F6-3) were produced during the same dolomitization episode. It also formed during 271.3–248.0 Ma in the Southwestern Sichuan Basin (Figure 2d) [70,95], corresponding to the late Permian, which was earlier than that in the Northwestern Sichuan Basin (240.0–202.0 Ma, the middle–late Triassic, Figure 2b) [65,66,96]. Depending on the U-Pb data, the dolostone was interpreted as being associated with the late Permian Emeishan Large Igneous Province (ELIP) in the Central and Southwestern Sichuan Basin [45,97], and with the late Triassic Longmenshan thrust in the Northwest Sichuan Basin [65,98]. More significantly, this indicates that the dolostone reservoir in the Central and Southwestern Sichuan Basin experienced cementation followed by dolomitization [27] during penecontemporaneous to shallow burial, at depths less than 700 m.

Although previous studies agreed on the hydrothermal origin of the Qixia dolostone in the study area [27,74,75], which factors control the dolostone distribution are still under discussion. Several factors, including the sedimentary facies (shoal facies) [27,64], basement faults [70,75,98], and E–W-trending strike–slip faults [99], are proposed to control the dolostone distribution. Some researchers proposed that the dolostones are majorly present in the top and middle part, which seems to be bedding-parallel, and this distribution has been interpreted to be controlled by the distribution of shoal facies [37,64,100]. However, this bedding-parallel facies-control model appears inconsistent with the actual distribution of the Qixia dolostone in our study. For instance, some wells, including the wells MX117 and MX108, show dolostones present in any position of the [65,98] grain-supported limestone unit rather than the top and middle part, and it is worth noting that these wells are generally located close to the faults (Figure 1b). Meanwhile, they also proposed that the grainstones, which are generally developed in high-energy shoals, were principally dolomitized due to their high porosities and permeabilities [72,101]. However, this is inconsistent with the lithological characteristics of the Qixia dolostone. Although the dolostones are generally fabric-destructive, our observation reveals that the dolostone layers can be interbedded within the packstone (F3), packstone–grainstone (F4), and even wackestone (F2) (Figures 6 and 7). Moreover, the bioclastic ghosts in dolostones include calcareous algae, echinoderm debris, fusulinids, and shell debris, also suggesting that the precursor limestone may be dominantly F3 and/or F4 (Figure 4f–h). Theoretically, the

dolomitization reaction generally starts in fine-grained sediments (e.g., carbonate mud) due to their high reaction surface [102,103], and preferential dolomitization of a specific carbonate layer requires its permeability to be two orders of magnitude higher than that of the surrounding rocks [104]. Relative to packstones, grainstones contain less carbonate mud yet lack significantly greater permeability [105], and calcite cements are common in F4 (Figure 4d). Under cathodoluminescence, the bioclasts and calcite cements in F4 show similar dull red luminescence (Figure 5a,b), while dolomite crystals display distinct luminescence (Figure 5c–h). This suggests that the cements and bioclasts formed in a similar depositional environment and are thus penecontemporaneous, with dolomitization occurring later. Therefore, we propose that the dolomitization in the Qixia Formation is not exclusive to high-energy grainstones. Instead, it affects a range of grain-supported lithologies, including F3 and F4.

Furthermore, some researchers have proposed that the dolostone is controlled by basement faults in the study area [63,65,91], because this phenomenon was demonstrated in the Southwestern and Northwestern Sichuan Basin [88,92]. However, recent studies suggest it distributes along E–W-trending strike–slip faults [93]. In this study, dolostone thickness was mapped (Figures 1b and 8e and Table A1), and the relationship between dolostone thickness and distances to faults (Figure 8e and Table A1) shows the dolostone predominantly occurs along E–W-trending strike–slip faults. Moreover, the strike–slip faults were reactivated during the middle–late Permian [42], a timeframe that overlaps with the dolomite U-Pb data (Figure 2c). Thus, based on lithological and geochronological data from the Qixia dolostone, we interpret it as having formed shortly after deposition and during shallow burial, with its distribution controlled primarily by fluid pathways associated with E–W-trending strike–slip faults. However, given the strong heterogeneity of Qixia dolostone, it cannot be excluded that primary sedimentary features, such as shoal distribution, locally influenced the pathways and efficiency of hydrothermal fluid migration.

5.2. How Does Dolomitization Influence Reservoir Quality?

The interpretations in this study are derived from the integration of data across multiple scales (full-diameter core, plug, and thin-section). It is acknowledged that each analytical technique has inherent limitations in representativity and resolution. For instance, plug-based MICP analysis provides precise pore–throat size distributions but may not capture full reservoir heterogeneity, while high-resolution μ-CT imaging is constrained by its limited field of view. In the case of F6-3, only one MICP sample yielded usable data, making complementary methods particularly necessary. The strength of our approach lies in leveraging the complementary nature of these datasets: larger-scale geological contexts from core and thin-section observations ground and validate the quantitative measurements from smaller-scale analyses, thereby constructing a more robust and three-dimensional understanding of the pore systems.

In the study area, porosities measured in plug samples (2.5 cm diameter × 5.0 cm height) show that dolostones are more porous than limestones (Figure 10a–c). The pores in dolostones may be inherited from precursor limestones [106], or be created during dolomitization [107,108]. The fact that dolostone porosities mainly fall within the higher range of limestone porosities (Figure 10a) is consistent with the inheritance model. This is further supported by the observation that some intercrystalline pores are actually moldic pores in precursor limestones [59] (Figure 9h). Therefore, the higher porosity in dolostones relative to limestones suggests that the compaction-resistant effect of dolostones may be important.

Meanwhile, evidence suggests that dolomitization may also contribute to the increase in porosity of the dolostone. Firstly, dolostone with larger dolomite crystals (F6-3) shows

higher porosities (plug samples) and dolomite contents than in F6-1 and F6-2 (Figure 10e), suggesting dolostone porosities increase with dolomite contents. Secondly, vugs and fractures, which are generally not included in the plug samples due to their large sizes, are exclusively observed in F6-3 (Figures 3h, 9b,c and 13g,h), suggesting the fracturing and dissolution accompanied with hydrothermal dolomitization may contribute to the increase in porosity. Lastly, the μ-CT of the full-diameter core sample of F6-3 shows large pores of 1000–10,000 μm, which exceeds the general sizes of primary pores and moldic pores in precursor limestones (Figure 9d,e). These suggest the dolomite crystal size and pores increase with the degree of hydrothermal dolomitization degree; therefore, hydrothermal dolomitization enhanced the reservoir porosity. However, it is worth noting that the median porosity value of F6-3 (approximately 5%, Figure 10e) does not exceed the P50 porosity of carbonate reservoirs at burial depth > 4.25 km (approximately 8%) documented by Ehrenberg and Nadeau [109]. Considering that the Qixia limestone was dolomitized during near-syndepositional to shallow burial conditions and subsequently experienced deep burial (up to 8000 m [27]), this lower-than-expected porosity may be attributed to two factors: (1) The pores formed during hydrothermal dolomitization are also significantly altered by deep burial diagenesis; and (2) some large pores/vugs are not included in the porosities measured in the plug samples.

Besides total porosity, reservoir quality is fundamentally governed by pore structures, which include pore size, throat size, and pore–throat connectivity [110–112], all of which collectively control permeability [113–116]. In hydrothermal dolomite systems, fractures are established as high-conductivity pathways that enhance permeability [112]. Core observations, along with the high permeability but low porosity of some plug samples, confirm their local role (Figure 10a,c). However, this study emphasizes an equally critical and complementary mechanism: the enhancement of matrix pore–throat networks during dolomitization. Even where major fractures are absent, dolomitization substantially improves permeability. This is demonstrated by two key observations. First, matrix-based plug samples from dolostones, especially facies F6-2 and F6-3, show systematically higher permeability than limestone samples (Figure 10d), despite the deliberate avoidance of fractures and large vugs during sampling. Second, MICP and μ—CT analyses show that F6-2 and F6-3 possess larger pore sizes and throat radii (Figures 12c–d, 13e–h and 14c–e,g) and higher pore coordination numbers than the other facies (Figure 14g,h). This optimized pore architecture provides a direct explanation for their superior permeability. Therefore, we conclude that hydrothermal dolomitization enhances permeability through two synergistic mechanisms: fracture development and systematic improvement of the matrix pore–throat network. By focusing on matrix-dominated samples, this study provides direct quantitative evidence that pore–throat enlargement and connectivity enhancement represent an inherent and major driver of permeability increase in hydrothermal dolostones, independent of fracture contribution.

6. Conclusions

This study integrates core observations, thin-section petrography, MICP, and μ-CT analyses to investigate the controlling factors of dolostone distribution and their impact on reservoir quality in the Qixia Formation, Central Sichuan Basin. The principal findings are as follows:

(1) Petrological analyses identify six lithofacies in the Qixia Formation: mudstone (F1), wackestone (F2), packstone (F3), packstone–grainstone (F4), rudstone (F5), and dolostone (F6). Based on dolomite crystal size and texture, F6 is subdivided into F6-1, F6-2, and F6-3.

(2) Strike–slip faults controlled the distribution of F6. Thick dolostone intervals are spatially associated with E–W-trending strike–slip faults, with thickness decreasing systematically away from fault zones. U-Pb dating results (267.9–263.0 Ma) coincide with the active period of these strike–slip faults, confirming their role as primary conduits for hydrothermal fluid flow.
(3) Reservoir porosity reflects both the inheritance of precursor pores and enhancement during hydrothermal dolomitization. Higher dolomitization intensity correlates with larger crystals and increased porosity.
(4) Hydrothermal dolomitization enhances permeability through two synergistic mechanisms: fracture development and systematic improvement of the matrix pore–throat network. Even in fracture-avoiding and vug-avoiding matrix samples, F6-2 and F6-3 exhibit higher permeability than limestones, with larger pore–throat radii and higher coordination numbers. This indicates that pore–throat network optimization is an inherent, fracture-independent permeability enhancement mechanism, and it plays an important role in controlling reservoir quality.

Author Contributions: Conceptualization, X.Z., H.Q., L.Z., Z.L. and H.X.; Data curation, X.Z., H.Q., L.Z., X.F., Z.L. and H.X.; Formal analysis, X.Z., H.Q., L.Z., X.F., Z.L. and Y.Z.; Funding acquisition, H.Q.; Investigation, X.Z., H.Q., D.Y. and H.X.; Methodology, X.Z., H.Q., L.Z., Z.L. and Y.Z.; Project administration, H.Q.; Supervision, H.Q.; Validation, H.Q.; Visualization, X.Z.; Writing—original draft, X.Z., H.Q., L.Z., Z.L. and D.Y.; Writing—review and editing, X.Z., H.Q., L.Z., X.F. and Z.L. All authors have read and agreed to the published version of the manuscript.

Funding: This research was funded by the National Key Research and Development Program of China (No. 2025YFE0212900) and the National Natural Science Foundation of China (No. 41702163).

Data Availability Statement: The raw data supporting the conclusions of this article will be made available by the authors on request.

Acknowledgments: We sincerely thank the reviewers and the editors for their valuable comments and thoughtful guidance. We deeply appreciate their time and effort, which have significantly improved the quality of our manuscript.

Conflicts of Interest: Authors Lianjin Zhang, Dongfan Yang and Huilin Xu are employed by the PetroChina Southwest Oil and Gas Field Company. The remaining authors declare that the research was conducted in the absence of any commercial or financial relationships that could be construed as potential conflicts of interest.

Appendix A

Table A1. Dolostone thickness in wells by distance to strike–slip fault.

No.	Dolostone Thickness in Well (m)	Distance to Adjacent Strike–Slip Fault (m)
1	0	8564
2	0	5347
3	0	4595
4	0	4098
5	0	3825
6	0	3520
7	0	3416
8	0	3260
9	0	3210
10	0	2992

Table A1. *Cont.*

No.	Dolostone Thickness in Well (m)	Distance to Adjacent Strike–Slip Fault (m)
11	0	2800
12	0	2456
13	0	2436
14	0	2336
15	0	2218
16	0	2181
17	0	2062
18	0	2052
19	0	2044
20	0	1967
21	0	1937
22	0	1827
23	0	1793
24	0	1775
25	0	1605
26	0	1595
27	0	1595
28	0	1558
29	0	1463
30	0	1352
31	0	1344
32	0	1267
33	0	1266
34	0	1226
35	0	1202
36	0	1134
37	0	1124
38	0	1114
39	0	1087
40	0	1012
41	0	969
42	0	963
43	0	943
44	0	939
45	0	866
46	0	865
47	0	832
48	0	810
49	0	805
50	0	788
51	0	766
52	0	762
53	0	742
54	0	721
55	0	677
56	0	646
57	0	607
58	0	575
59	0	567
60	0	560
61	0	486
62	0	480

Table A1. *Cont.*

No.	Dolostone Thickness in Well (m)	Distance to Adjacent Strike–Slip Fault (m)
63	0	479
64	0	471
65	0	450
66	0	426
67	0	370
68	0	348
69	0	330
70	0	278
71	0	229
72	0	225
73	0	188
74	0	160
75	0	154
76	0	106
77	0	94
78	0	93
79	0	36
80	0	30
81	0	8
82	0.1	1661
83	0.1	1324
84	0.1	362
85	0.2	951
86	0.3	2456
87	0.3	2078
88	0.3	1616
89	0.3	767
90	0.4	2887
91	0.4	373
92	0.4	6105
93	0.4	2975
94	0.4	2276
95	0.4	1289
96	0.4	1157
97	0.5	3766
98	0.5	4173
99	0.5	4175
100	0.5	1500
101	0.5	428
102	0.6	1516
103	0.6	3379
104	0.6	770
105	0.6	1510
106	0.6	4264
107	0.6	1252
108	0.6	317
109	0.6	296
110	0.6	4092
111	0.8	2302
112	0.9	3389
113	0.9	1308
114	0.9	3248

Table A1. *Cont.*

No.	Dolostone Thickness in Well (m)	Distance to Adjacent Strike–Slip Fault (m)
115	1.0	4946
116	1.0	4880
117	1.0	586
118	1.1	2959
119	1.1	685
120	1.1	622
121	1.1	549
122	1.1	424
123	1.1	232
124	1.2	1195
125	1.3	2614
126	1.3	1404
127	1.3	717
128	1.3	698
129	1.3	1094
130	1.3	1206
131	1.4	2741
132	1.4	94
133	1.5	1006
134	1.5	2635
135	1.5	979
136	1.6	1356
137	1.6	1971
138	1.6	963
139	1.6	194
140	1.6	4771
141	1.6	482
142	1.8	3089
143	1.8	2935
144	1.8	1353
145	1.9	877
146	1.9	838
147	1.9	3770
148	1.9	442
149	2.0	594
150	2.0	1487
151	2.1	330
152	2.1	1489
153	2.1	1205
154	2.3	2354
155	2.3	1188
156	2.4	1187
157	2.5	708
158	2.5	273
159	2.6	1590
160	2.6	4848
161	2.7	31
162	2.8	450
163	2.9	350
164	2.9	1370
165	3.0	2746
166	3.0	1050
167	3.1	5280

Table A1. *Cont.*

No.	Dolostone Thickness in Well (m)	Distance to Adjacent Strike–Slip Fault (m)
168	3.1	503
169	3.1	320
170	3.2	767
171	3.2	499
172	3.4	437
173	3.4	1706
174	3.5	514
175	3.8	1341
176	4.0	635
177	4.0	835
178	4.3	4282
179	4.4	1997
180	4.4	24
181	4.5	2805
182	4.6	922
183	4.8	1939
184	5.0	1265
185	5.1	1538
186	5.3	1915
187	5.3	3631
188	5.3	794
189	5.5	161
190	5.5	137
191	5.5	1015
192	5.7	131
193	6.0	4700
194	6.2	2562
195	6.2	110
196	6.3	242
197	6.3	4244
198	6.5	146
199	6.7	852
200	6.9	599
201	7.0	85
202	7.0	2565
203	7.2	1606
204	7.3	811
205	7.3	1383
206	7.3	893
207	7.3	507
208	7.8	3616
209	8.5	2953
210	8.5	337
211	8.5	1666
212	8.7	1321
213	8.9	2078
214	9.1	800
215	9.1	807
216	10.2	1408
217	10.3	9
218	10.6	840
219	11.2	1275
220	11.2	16

Table A1. *Cont.*

No.	Dolostone Thickness in Well (m)	Distance to Adjacent Strike–Slip Fault (m)
221	12.0	289
222	14.9	1898
223	15.3	1296
224	16.2	1515
225	17.3	1267

Table A2. Porosity and permeability data of Qixia Formation carbonate rocks in the study area.

No.	Lithofacies	Porosity (%)	Permeability (mD)
1	F1	0.4	0.00068
2	F1	0.9	0.00292
3	F2	0.5	0.00017
4	F2	1.0	0.10300
5	F2	1.4	0.00012
6	F2	1.8	0.00019
7	F2	4.1	0.01587
8	F3	0.1	0.00002
9	F3	0.4	0.00012
10	F3	0.4	0.00008
11	F3	0.4	0.00016
12	F3	0.5	0.00110
13	F3	0.6	0.00011
14	F3	0.8	0.00184
15	F3	0.9	0.00779
16	F3	1.0	0.00022
17	F3	1.1	0.00111
18	F3	1.3	0.00009
19	F3	1.4	0.00212
20	F3	1.6	0.07098
21	F3	1.7	0.00037
22	F3	2.2	0.00043
23	F3	2.4	0.00109
24	F3	2.6	0.00058
25	F3	2.6	0.00016
26	F3	2.8	0.00107
27	F3	3.1	0.00099
28	F3	3.5	0.00089
29	F3	3.8	0.00538
30	F4	0.4	0.00150
31	F4	0.4	0.02960
32	F4	0.4	0.00008
33	F4	0.4	0.00021
34	F4	0.6	0.00006
35	F4	0.6	0.00016
36	F4	0.6	0.00022
37	F4	0.6	0.00965
38	F4	0.7	0.00018
39	F4	0.8	0.00011
40	F4	0.8	0.00005
41	F4	1.0	0.00011
42	F4	1.0	0.00024
43	F4	1.1	0.00008

Table A2. *Cont.*

No.	Lithofacies	Porosity (%)	Permeability (mD)
44	F4	1.1	0.00098
45	F4	1.2	0.19700
46	F4	1.3	0.00012
47	F4	1.3	3.15000
48	F4	1.4	0.00175
49	F4	1.6	0.00063
50	F4	1.7	0.00067
51	F4	1.8	0.00068
52	F4	1.8	0.01060
53	F4	2.1	0.00140
54	F4	2.1	0.00003
55	F4	2.3	0.00096
56	F4	2.3	0.00227
57	F4	2.6	0.00039
58	F4	3.0	0.00044
59	F4	3.6	0.68100
60	F4	3.7	0.01723
61	F4	4.2	0.00251
62	F5	1.4	0.94200
63	F5	1.8	0.02120
64	F6-1	2.5	0.00151
65	F6-1	3.9	2.80890
66	F6-2	2.2	0.00153
67	F6-2	2.3	0.02860
68	F6-2	2.4	0.00115
69	F6-2	2.5	0.00375
70	F6-2	2.7	0.00080
71	F6-2	2.9	0.00900
72	F6-2	2.9	0.00887
73	F6-2	3.2	0.03070
74	F6-2	3.5	0.00376
75	F6-2	3.7	0.01630
76	F6-2	3.7	0.15290
77	F6-2	4.0	0.01540
78	F6-2	4.0	0.13110
79	F6-2	5.6	0.48100
80	F6-2	6.8	0.05200
81	F6-2	9.4	0.18000
82	F6-3	2.3	0.03590
83	F6-3	2.3	0.00209
84	F6-3	2.3	0.00482
85	F6-3	2.8	2.78000
86	F6-3	3.7	0.00277
87	F6-3	4.1	1.75000
88	F6-3	4.1	0.00836
89	F6-3	4.8	0.01510
90	F6-3	6.3	0.01570
91	F6-3	6.7	0.06344
92	F6-3	7.7	0.15700
93	F6-3	9.2	2.55000

References

1. Schmoker, J.W.; Krystinik, K.B.; Halley, R.B. Selected Characteristics of Limestone and Dolomite Reservoirs in the United States. *AAPG Bull.* **1985**, *69*, 733–741. [CrossRef]

2. Ma, F.; Yang, L.; Gu, J.; Chen, X.; Zhao, Z.; Jin, Y.; Gao, L. The Summary on Exploration of the Dolomite Oilfields in the World. *Acta Sedimentol. Sin.* **2011**, *29*, 1010–1021. (In Chinese with English Abstract)
3. Barbier, M.; Floquet, M.; Hamon, Y.; Callot, J.P. Nature and distribution of diagenetic phases and petrophysical properties of carbonates: The Mississippian Madison Formation (Bighorn Basin, Wyoming, USA). *Mar. Pet. Geol.* **2015**, *67*, 230–248. [CrossRef]
4. Noorian, Y.; Moussavi-Harami, R.; Hollis, C.; Reijmer, J.J.G.; Mahboubi, A.; Omidpour, A. Control of climate, sea-level fluctuations and tectonics on the pervasive dolomitization and porosity evolution of the Oligo-Miocene Asmari Formation (Dezful Embayment, SW Iran). *Sediment. Geol.* **2022**, *427*, 106048. [CrossRef]
5. Murray, R.C. Origin of porosity in carbonate rocks. *J. Sediment. Petrol.* **1960**, *30*, 59–84. [CrossRef]
6. Sun, S.Q. Dolomite Reservoirs: Porosity Evolution and Reservoir Characteristics. *AAPG Bull.* **1995**, *79*, 186–204. [CrossRef]
7. Weyl, P.K. Porosity through dolomitization—Conservation-of-mass requirements. *J. Sediment. Res.* **1960**, *30*, 85–90. [CrossRef]
8. Koeshidayatullah, A.; Corlett, H.; Stacey, J.; Swart, P.K.; Boyce, A.; Hollis, C. Origin and evolution of fault-controlled hydrothermal dolomitization fronts: A new insight. *Earth Planet. Sci. Lett.* **2020**, *541*, 116291. [CrossRef]
9. Wendte, J.; Byrnes, A.; Sargent, D. The control of hydrothermal dolomitization and associated fracturing on porosity and permeability of reservoir facies of the Upper Devonian Jean Marie Member (Redknife Formation) in the July Lake area of northeastern British Columbia. *Bull. Can. Pet. Geol.* **2009**, *57*, 387–408. [CrossRef]
10. Lee, E.Y.; Kominz, M.; Reuning, L.; Gallagher, S.J.; Takayanagi, H.; Ishiwa, T.; Knierzinger, W.; Wagreich, M. Quantitative compaction trends of Miocene to Holocene carbonates off the west coast of Australia. *Aust. J. Earth Sci.* **2021**, *68*, 1149–1161. [CrossRef]
11. Choquette, P.W.; Steinen, R.P. *Mississippian Non-Supratidal Dolomite, Ste. Genevieve Limestone, Illinois Basin: Evidence for Mixed-Water Dolomitization*; SEPM Society for Sedimentary Geology: Houston, TX, USA, 1980.
12. Ehrenberg, S.N.; Eberli, G.P.; Keramati, M.; Moallemi, S.A. Porosity-permeability relationships in interlayered limestone-dolostone reservoirs. *AAPG Bull.* **2006**, *90*, 91–114. [CrossRef]
13. Moore, C.H.; Druckman, Y. Burial Diagenesis and Porosity Evolution, Upper Jurassic Smackover, Arkansas and Louisiana. *AAPG Bull.* **1981**, *65*, 597–628. [CrossRef]
14. Davies, G.R.; Smith, L.B., Jr. Structurally controlled hydrothermal dolomite reservoir facies: An overview. *AAPG Bull.* **2006**, *90*, 1641–1690. [CrossRef]
15. Dewit, J.; Huysmans, M.; Muchez, P.; Hunt, D.W.; Thurmond, J.B.; Verges, J.; Saura, E.; Fernandez, N.; Romaire, I.; Esestime, P.; et al. Reservoir characteristics of fault-controlled hydrothermal dolomite bodies: Ramales Platform case study. *Adv. Carbonate Explor. Reserv. Anal.* **2012**, *370*, 83–109. [CrossRef]
16. Ronchi, P.; Masetti, D.; Tassan, S.; Camocino, D. Hydrothermal dolomitization in platform and basin carbonate successions during thrusting: A hydrocarbon reservoir analogue (Mesozoic of Venetian Southern Alps, Italy). *Mar. Pet. Geol.* **2012**, *29*, 68–89. [CrossRef]
17. Shi, L.; Lu, Z.; Li, F.; Qing, H.; Jiang, W.; Li, W.; Li, Z.; Ye, N.; Zhu, B.; Tang, Q.; et al. Depositional systems constraining the distribution of hydrothermal dolostone geobodies: A case study of Permian Guadalupian dolostone in the eastern Sichuan Basin. *Sediment. Geol.* **2025**, *479*, 106837. [CrossRef]
18. Ye, N.; Zhang, S.; Qing, H.; Li, Y.; Huang, Q.; Liu, D. Dolomitization and its impact on porosity development and preservation in the deeply burial Lower Ordovician carbonate rocks of Tarim Basin, NW China. *J. Pet. Sci. Eng.* **2019**, *182*, 106303. [CrossRef]
19. Hollis, C.; Bastesen, E.; Boyce, A.; Corlett, H.; Gawthorpe, R.; Hirani, J.; Rotevatn, A.; Whitaker, F. Fault-controlled dolomitization in a rift basin. *Geology* **2017**, *45*, 219–222. [CrossRef]
20. Qing, H.; Mountjoy, E.W. Formation of Coarsely Crystalline, Hydrothermal Dolomite Reservoirs in the Presqu'ile Barrier, Western Canada Sedimentary Basin. *AAPG Bull.* **1994**, *78*, 55–77. [CrossRef]
21. Mansurbeg, H.; Alsuwaidi, M.; Morad, D.; Morad, S.; Tiepolo, M.; Shahrokhi, S.; Al-Aasm, I.S.; Koyi, H. Disconformity-controlled hydrothermal dolomitization and cementation during basin evolution: Upper Triassic carbonates, UAE. *Geology* **2024**, *52*, 486–491. [CrossRef]
22. Mansurbeg, H.; Alsuwaidi, M.; Salih, N.; Shahrokhi, S.; Morad, S. Integration of stable isotopes, radiometric dating and microthermometry of saddle dolomite and host dolostones (Cretaceous carbonates, Kurdistan, Iraq): New insights into hydrothermal dolomitization. *Mar. Pet. Geol.* **2021**, *127*, 104989. [CrossRef]
23. Martín-Martín, J.D.; Gomez-Rivas, E.; Bover-Arnal, T.; Travé, A.; Salas, R.; Moreno-Bedmar, J.A.; Tomás, S.; Corbella, M.; Teixell, A.; Vergés, J.; et al. The Upper Aptian to Lower Albian syn-rift carbonate succession of the southern Maestrat Basin (Spain): Facies architecture and fault-controlled stratabound dolostones. *Cretac. Res.* **2013**, *41*, 217–236. [CrossRef]
24. Lavoie, D.; Chi, G.; Brennan-Alpert, P.; Desrochers, A.; Bertrand, R. Hydrothermal dolomitization in the Lower Ordovician Romaine Formation of the Anticosti Basin: Significance for hydrocarbon exploration. *Bull. Can. Pet. Geol.* **2005**, *53*, 454–471. [CrossRef]
25. Mohammed Sajed, O.K.; Glover, P.W.J. Dolomitization, cementation and reservoir quality in three Jurassic and Cretaceous carbonate reservoirs in north-western Iraq. *Mar. Pet. Geol.* **2020**, *115*, 104256. [CrossRef]

26. Sheng, K.; Wang, Y.; Cao, Y.; Wang, S.; Wang, Y.; Ma, S.; Du, Y. Influence of multistage hydrothermal fluids on dolomite reservoirs: A case study from the Lower Ordovician Yeli-Liangjiashan Formation in the Chengdao-Zhuanghai area, Jiyang subbasin, Bohai Bay Basin, China. *GSA Bull.* **2023**, *136*, 2111–2136. [CrossRef]
27. Bai, X.; Wen, L.; Zhang, Y.; Zhang, X.; Wang, J.; Chen, Y.; Peng, S.; Wang, W.; Zhong, J.; Li, Y.; et al. Origin of facies-controlled dolomite and exploration significance of the Middle Permian Qixia Formation in Central Sichuan Basin, Western China. *Pet. Sci.* **2024**, *21*, 2927–2945. [CrossRef]
28. Jiang, Y.; Gu, Y.; Li, K.; Li, S.; Luo, M.; He, B. Space types and origins of hydrothermal dolomite reservoirs in the Middle Permian strata, Central Sichuan Basin. *Nat. Gas Ind.* **2018**, *38*, 16–24. (In Chinese with English Abstract)
29. Gu, Z.; Lonergan, L.; Zhai, X.; Zhang, B.; Lu, W. The formation of the Sichuan Basin, South China, during the Late Ediacaran to Early Cambrian. *Basin Res.* **2021**, *33*, 2328–2357. [CrossRef]
30. Liu, S.; Yang, Y.; Deng, B.; Zhong, Y.; Wen, L.; Sun, W.; Li, Z.; Jansa, L.; Li, J.; Song, J.; et al. Tectonic evolution of the Sichuan Basin, Southwest China. *Earth-Sci. Rev.* **2021**, *213*, 103470. [CrossRef]
31. Wang, J.; Li, Z.-X. History of Neoproterozoic rift basins in South China: Implications for Rodinia break-up. *Precambrian Res.* **2003**, *122*, 141–158. [CrossRef]
32. Shi, S.; Yang, W.; Zhou, G.; Jiang, H.; Meng, H.; Wu, S.; Zhang, Y.; Lu, W.; Bai, Z. Impact of Tethyan domain evolution on the formation of petroleum systems in the Sichuan super basin, SW China. *Pet. Explor. Dev.* **2024**, *51*, 1024–1039. [CrossRef]
33. Li, G.; Li, Z.; Li, D.; Liu, H.; Su, G.; Yan, S. Basement fault control on the extensional process of a basin: A case study from the Cambrian–Silurian of the Sichuan Basin, South-west China. *Geol. J.* **2022**, *57*, 3648–3667. [CrossRef]
34. Huang, H.; He, D.; Li, Y.; Li, J.; Zhang, L. Silurian tectonic-sedimentary setting and basin evolution in the Sichuan area, southwest China: Implications for palaeogeographic reconstructions. *Mar. Pet. Geol.* **2018**, *92*, 403–423. [CrossRef]
35. Su, G.; Li, Z.; Ying, D.; Li, G.; Ying, W. Formation and evolution of the Caledonian paleo-uplift and its genetic mechanism in the Sichuan Basin. *ACTA Geol. Sin.* **2020**, *94*, 1793–1812. (In Chinese with English Abstract)
36. Huang, H.; He, D.; Li, Y.; Wang, B. The prototype and its evolution of the Sichuan sedimentary basin and adjacent areas during Liangshan and Qixia stages in Permian. *Acta Petrol. Sin.* **2017**, *33*, 1317–1337. (In Chinese with English Abstract)
37. Li, M.; Tan, X.; Yang, Y.; Ni, H.; Luo, B.; Wen, L.; Zhang, B.; Xiao, D.; Xu, Q. Sequence-lithofacies paleogeographic characteristics and petroleum geological significance of Lower Permian Qixia Stage in Sichuan Basin and its adjacent areas, SW China. *Pet. Explor. Dev.* **2022**, *49*, 1295–1309. [CrossRef]
38. Liu, H.; Chen, P.; Wu, D.; Fu, M.; Deng, H.; He, P. Sedimentary Models of Qixia Formation in Gaoshiti-Moxi Area of Sichuan Basin. *Sci. Technol. Eng.* **2023**, *23*, 6760–6774. (In Chinese with English Abstract)
39. Dong, Y.; Chen, H.; Wang, J.; Hou, M.; Xu, S.; Zhu, P.; Zhang, C.; Cui, Y. Thermal convection dolomitization induced by the Emeishan Large Igneous Province. *Mar. Pet. Geol.* **2020**, *116*, 104308. [CrossRef]
40. Feng, Q.; Qiu, N.; Fu, X.; Li, W.; Liu, X.; Ji, R. Maturity evolution of Permian source rocks in the Sichuan Basin, southwestern China: The role of the Emeishan mantle plume. *J. Asian Earth Sci.* **2022**, *229*, 105180. [CrossRef]
41. Feng, Q.; Qiu, N.; Fu, X.; Li, W.; Xu, Q.; Li, X.; Wang, J. Permian geothermal units in the Sichuan Basin: Implications for the thermal effect of the Emeishan mantle plume. *Mar. Pet. Geol.* **2021**, *132*, 105226. [CrossRef]
42. Chen, Z.; Li, W.; Wang, L.; Lei, Y.; Yang, G.; Zhang, B.; Yin, H.; Yuan, B. Structural geology and favorable exploration prospect belts in northwestern Sichuan Basin, SW China. *Pet. Explor. Dev.* **2019**, *46*, 413–425. [CrossRef]
43. He, L. Permian to Late Triassic evolution of the Longmen Shan Foreland Basin (Western Sichuan): Model results from both the lithospheric extension and flexure. *J. Asian Earth Sci.* **2014**, *93*, 49–59. [CrossRef]
44. Shi, Z.; Zhou, T.; Guo, C. Clastic sedimentary records of the Upper Triassic Sichuan Basin, China: Implications for the transition from marine to transitional environment. *Geol. J.* **2022**, *57*, 4393–4411. [CrossRef]
45. Feng, K.; Xu, S.; Chen, A.; Ogg, J.; Hou, M.; Lin, L.; Chen, H. Middle Permian dolomites of the SW Sichuan Basin and the role of the Emeishan Large Igneous Province in their origin. *Mar. Pet. Geol.* **2021**, *128*, 104981. [CrossRef]
46. Hu, A.; Pan, L.; Hao, Y.; Shen, A.; Gu, M. Origin, Characteristics and Distribution of Dolostone Reservoir in Qixia Formation and Maokou Formation, Sichuan Basin, China. *Mar. Orig. Pet. Geol.* **2018**, *23*, 39–52. (In Chinese with English Abstract)
47. Duan, J.; Zheng, J.; Luo, X.; Wang, Y.; Hao, Y. Micro-area geochemical constraints on the diagenesis and hydrocarbon accumulation history of dolomite reservoir of the Middle Permian Qixia Formation in northwest Sichuan Basin and its significance. *China Pet. Explor.* **2022**, *27*, 162–180. (In Chinese with English Abstract)
48. Li, L.; Zhang, Z.; Li, M.; Ni, J.; Geng, C.; Tang, S.; Yang, W.; Tan, X. Sequence stratigraphic characteristics and favorable reservoirs distribution of Permian Qixia Stage in Weiyuan-Gaoshiti area, Sichuan Basin. *Lithol. Reserv.* **2022**, *34*, 32–46. (In Chinese with English Abstract)
49. Tang, Y.; Li, L.; Tan, X.; Li, M.; Lu, F.; Zhang, B. Sequence Stratigraphy and Lithofacies Paleogeography of the Early Permian Qixia Stage in Southwestern Sichuan Basin. *Acta Sedimentol. Sin.* **2024**, *42*, 575–592. (In Chinese with English Abstract)
50. Guan, S.; Zhang, Y.; Jiang, H.; Lu, X.; Liang, H.; Huang, S.; Zhu, G.; Ren, R.; Su, N. Cratonic strike-slip fault systems in the Central Sichuan Basin, China. *Earth-Sci. Rev.* **2024**, *254*, 104800. [CrossRef]

51. Ma, B.; Liang, H.; Wu, G.; Tang, Q.; Tian, W.; Zhang, C.; Yang, S.; Zhong, Y.; Zhang, X.; Zhang, Z. Formation and evolution of the strike-slip faults in the Central Sichuan Basin, SW China. *Pet. Explor. Dev.* **2023**, *50*, 373–387. [CrossRef]
52. Li, Y.; Bian, C.; Li, S.; Liu, G.; Sun, W.; Zhang, L.; Li, Z. Discovery of deep strike-slip faults and its exploration significance in Zitong area, western Sichuan Basin. *Chin. J. Geol.* **2023**, *58*, 36–50. (In Chinese with English Abstract)
53. Tian, F.; Liang, H.; Zang, D.; Liu, H.; Wu, F.; He, D.; Liu, P.; Liu, Z.; Zhang, W.; Si, Y.; et al. Structural characteristics of strike-slip faults in the Luzhou-Yunjin area, southern Sichuan Basin. *Chin. J. Geol.* **2024**, *59*, 804–818. (In Chinese with English Abstract)
54. Wu, Y.; Liu, J.; Feng, L.; Pang, Y.; Tang, Q.; Liu, X.; Wu, G. Characteristics of the strike-slip faults and their effects on the gas accumulation in the southeastern Kaijiang-Liangping trough, Sichuan Basin. *Mar. Orig. Pet. Geol.* **2023**, *28*, 291–300. (In Chinese with English Abstract)
55. Zeng, T.; Fan, R.; Xia, W.; Zou, Y.; Shi, S. Formation and evolution of strike-slip fault zones in the eastern Sichuan Basin and identification and characterization of the fault zones: A case study of the Fuling area. *Earth Sci. Front.* **2022**, *30*, 366–385. (In Chinese with English Abstract)
56. Wang, Z.; Zhao, W.; Li, Z.; Jiang, X.; Li, J. Role of basement faults in gas accumulation of Xujiahe Formation, Sichuan Basin. *Pet. Explor. Dev.* **2008**, *35*, 541–547. [CrossRef]
57. Pan, L.; Xu, Z.; Li, R.; Zou, Y. Basement Fault Characterization and Hydrocarbon Accumulation in Fuling of Southeastern Sichuan. *Spec. Oil Gas Reserv.* **2020**, *27*, 19–25. (In Chinese with English Abstract)
58. Yang, T.; Azmy, K.; He, Z.; Li, S.; Liu, E.; Wu, S.; Wang, J.; Li, T.; Gao, J. Fault-controlled hydrothermal dolomitization of Middle Permian in southeastern Sichuan Basin, SW China, and its temporal relationship with the Emeishan Large Igneous Province: New insights from multi-geochemical proxies and carbonate U–Pb dating. *Sediment. Geol.* **2022**, *439*, 106215. [CrossRef]
59. Jiang, Y.; Chen, S.; Li, W.; Liang, X.; Lei, T.; Min, J.; Chen, R. The development process and numerical simulation of strike-slip fault in Central Sichuan Basin. *Sci. Technol. Eng.* **2025**, *25*, 2253–2264. (In Chinese with English Abstract)
60. Ma, D.; Wang, Z.; Duan, S.; Gao, J.; Jiang, Q.; Jiang, H.; Zeng, F.; Lu, W. Strike-slip faults and their significance for hydrocarbon accumulation in Gaoshiti–Moxi area, Sichuan Basin, SW China. *Pet. Explor. Dev.* **2018**, *45*, 851–861. [CrossRef]
61. Lu, G.; Tian, F.; He, D.; Liu, H.; Zhao, X. Structural Characteristics and Evolution of No.9 Strike-Slip Fault Zone in Gaoshiti-Moxi Area in Central Sichuan Basin. *Earth Sci.* **2023**, *48*, 2238–2253. (In Chinese with English Abstract)
62. Shen, S.; Zhang, H.; Zhang, Y.; Yuan, D.; Chen, B.; He, W.; Mu, L.; Lin, W.; Wang, W.; Chen, J.; et al. Permian integrative stratigraphy and timescale of China. *Sci. China Earth Sci.* **2019**, *62*, 154–188. [CrossRef]
63. Shen, B.; Shen, S.; Hou, Z.; Wu, Q.; Zhang, S.; Zhang, B.; Zhang, Y.; Yuan, D. Lithostratigraphic subdivision and correlation of the Permian in China. *J. Stratigr.* **2021**, *45*, 319–339. (In Chinese with English Abstract)
64. He, J.; Lian, Z.; Luo, W.; Zhou, H.; Xu, H.; He, P.; Yang, Y.; Lan, X. Characteristics and main controlling factors of intra-platform shoal thin-layer dolomite reservoirs: A case study of Middle Permian Qixia Formation in Gaoshiti–Moxi area of Sichuan Basin, SW China. *Pet. Explor. Dev.* **2024**, *51*, 69–80. [CrossRef]
65. Pan, L.; Shen, A.; Zhao, J.; Hu, A.; Hao, Y.; Liang, F.; Feng, Y.; Wang, X.; Jiang, L. LA-ICP-MS U-Pb geochronology and clumped isotope constraints on the formation and evolution of an ancient dolomite reservoir: The Middle Permian of northwest Sichuan Basin (SW China). *Sediment. Geol.* **2020**, *407*, 105728. [CrossRef]
66. Pan, L.; Hao, Y.; Liang, F.; Hu, A.; Feng, Y.; Zhao, J. New evidence of laser in situ U-Pb dating and isotopic geochemistry for the genesis of dolomite reservoir: A case study of dolomite reservoir from Middle Permian Qixia Formation in northwestern Sichuan Basin. *Acta Pet. Sin.* **2022**, *43*, 223–233. (In Chinese with English Abstract)
67. He, W.; Meng, Q.; Yin, C.; Wang, X.; Zhang, H.; Shi, J. Geological characteristics and favorable exploration plays of gas in Qixia Formation dolomite in Hechuan-Tongnan area of Sichuan Basin. *Pet. Geol. Oilfield Dev. Daqing* **2022**, *41*, 1–11. (In Chinese with English Abstract)
68. Lu, X.; Gui, L.; Wang, Z.; Liu, S.; Liu, Q.; Fan, J.; Chen, W.; Ma, X.; Jiang, H.; Fu, X.; et al. Activity time of strike slip faults and their controlling effects on hydrocarbon accumulation in Central Sichuan Basin: Evidence from U-Pb dating and fluid inclusions of cements in fault zone. *Acta Pet. Sin.* **2024**, *45*, 642–658. (In Chinese with English Abstract)
69. Zhu, M.; Huang, S.; Song, X.; Wang, X.; Shi, J.; Tian, X.; Yao, Q.; Wang, H. Main controlling factors of the Middle Permian dolomite reservoir and prediction of exploration zone in Tongnan-Hechuan block, Sichuan Basin. *China Pet. Explor.* **2022**, *27*, 149–161. (In Chinese with English Abstract)
70. Xiao, D.; Huang, T.; Xu, Q.; Tan, X.; Wen, L.; Zheng, J.; Cao, J. Two pulsed activities of the Emeishan large igneous province in southwestern China inferred from dolomite U-Pb geochronology and significance. *Geol. Soc. Am. Bull.* **2024**, *136*, 3977–3992. [CrossRef]
71. Dickson, J.A.D. A modified staining technique for carbonates in thin section. *Nature* **1965**, *205*, 587. [CrossRef]
72. Duan, J.; Zheng, J.; Shen, A.; Zhu, M.; Yao, Q.; Hao, Y. Characteristics and genesis of dolomite reservoir of the Lower Permian Qixia Formation in Central Sichuan Basin. *Mar. Orig. Pet. Geol.* **2021**, *26*, 345–356. (In Chinese with English Abstract)
73. He, P.; Xu, W.; Zhang, L.; Fu, M.; Wu, D.; Deng, H.; Xu, H.; Sun, Q. Characteristics and Genetic Mechanism of Qixia Formation Dolomite in Moxi-Gaoshiti Area, Central Sichuan Basin. *Acta Pet. Sin.* **2021**, *39*, 1532–1545. (In Chinese with English Abstract)

74. Chen, X.; Zhao, W.; Zhang, L.; Zhao, Z.; Lu, Y.; Zhang, B.; Yang, Y. Discovery and exploration significance of structure-controlled hydrothermal dolomites in the Middle Permian of the Central Sichuan Basin. *Acta Pet. Sin.* **2012**, *33*, 562–569. (In Chinese with English Abstract)
75. Gao, J.; Zheng, H.; Liu, B.; Pan, L.; Li, R.; Wu, J.; Yang, X.; Tang, H.; Dong, Y. Genetic Mechanism of Structurally Controlled Dolomites Derived from Seawater-Hydrothermal Mixed Fluids—A Case Study from Middle Permian, Central Sichuan Basin, South China. *Minerals* **2023**, *13*, 758. [CrossRef]
76. Pan, L.; Hao, Y.; Liang, F. Hydrothermal modified dolomite reservoir of Qixia Formation in central Sichuan: Fluid activity time and structural background. In Proceedings of the 17th National Conference on Paleogeography and Sedimentology, Qingdao, China, 8 November 2023. (In Chinese with English Abstract)
77. Dunham, R.J. Classification of Carbonate Rocks According to Depositional Texture. In *Classification of Carbonate Rocks—A Symposium*; American Association of Petroleum Geologists: Tulsa, OK, USA, 1962; pp. 108–121.
78. Embry, A.F.; Klovan, J.E. A late Devonian reef tract on northeastern banks island. *Bull. Can. Pet. Geol.* **1971**, *19*, 730–781. [CrossRef]
79. Sibley, D.F.; Gregg, J.M. Classification of Dolomite Rock Textures. *J. Sediment. Res.* **1987**, *57*, 967–975. [CrossRef]
80. Choquette, P.W.; Pray, L.C. Geologic Nomenclature and Classification of Porosity in Sedimentary Carbonates. *AAPG Bull.* **1970**, *54*, 207–250. [CrossRef]
81. Ali, A.; Chiang, Y.W.; Santos, R.M. X-Ray Diffraction Techniques for Mineral Characterization: A Review for Engineers of the Fundamentals, Applications, and Research Directions. *Minerals* **2022**, *12*, 205. [CrossRef]
82. Shen, X.; Huang, Q.; Wang, C.; Wang, M.; Shan, Q. A preferred orientation correction of schistose minerals quantitative analysis via X-ray diffraction. *Miner. Eng.* **2025**, *230*, 109397. [CrossRef]
83. Xiao, J.; Song, Y.; Li, Y. Comparison of Quantitative X-ray Diffraction Mineral Analysis Methods. *Minerals* **2023**, *13*, 566. [CrossRef]
84. Drost, K.; Chew, D.; Petrus, J.A.; Scholze, F.; Woodhead, J.D.; Schneider, J.W.; Harper, D.A.T. An Image Mapping Approach to U-Pb LA-ICP-MS Carbonate Dating and Applications to Direct Dating of Carbonate Sedimentation. *Geochem. Geophys. Geosyst* **2018**, *19*, 4631–4648. [CrossRef]
85. Lu, X.; Gui, L.; Chen, W.; Liu, S.; Wu, S.; Fan, J.; Liu, Q.; Sun, J.; Zhang, L.; Xiao, Y.; et al. Improvement of in situ LA-ICP-MS U-Pb dating method for carbonate minerals and its application in petroleum geology. *Sci. China Earth Sci.* **2023**, *66*, 2914–2929. [CrossRef]
86. Liu, Y.; Liu, Y.; Zhang, Q.; Li, C.; Feng, Y.; Wang, Y.; Xue, Y.; Ma, H. Petrophysical static rock typing for carbonate reservoirs based on mercury injection capillary pressure curves using principal component analysis. *J. Pet. Sci. Eng.* **2019**, *181*, 106175. [CrossRef]
87. Nooruddin, H.A.; Hossain, M.E.; Al-Yousef, H.; Okasha, T. Comparison of permeability models using mercury injection capillary pressure data on carbonate rock samples. *J. Pet. Sci. Eng.* **2014**, *121*, 9–22. [CrossRef]
88. Washburn, E.W. Note on a Method of Determining the Distribution of Pore Sizes in a Porous Material. *Proc. Natl. Acad. Sci. USA* **1921**, *7*, 115–116. [CrossRef] [PubMed]
89. Abera, K.A.; Manahiloh, K.N.; Motalleb, N.M. The effectiveness of global thresholding techniques in segmenting two-phase porous media. *Constr. Build. Mater.* **2017**, *142*, 256–267. [CrossRef]
90. Cnudde, V.; Boone, M.N. High-resolution X-ray computed tomography in geosciences: A review of the current technology and applications. *Earth-Sci. Rev.* **2013**, *123*, 1–17. [CrossRef]
91. Schlüter, S.; Sheppard, A.; Brown, K.; Wildenschild, D. Image processing of multiphase images obtained via X-ray microtomography: A review. *Water Resour. Res.* **2014**, *50*, 3615–3639. [CrossRef]
92. Pei, S.; Wang, X.; Hu, X.; Li, R.; Long, H.; Huang, D. Characteristics and diagenetic evolution of dolomite reservoirs in the Middle Permian Qixia Formation, southwestern Sichuan Basin, China. *Carbonates Evaporites* **2022**, *37*, 17. [CrossRef]
93. Yang, Z.; Sun, H.; Zhong, D.; Zhang, B.; Liu, R.; Zeng, Y.; Chen, X.; Li, R.; Peng, S. Effects of basin tectonic evolution on multi-phase dolomitization: Insights from the Middle Permian Qixia Formation of the NW Sichuan Basin, SW China. *Sediment. Geol.* **2024**, *470*, 106718. [CrossRef]
94. Quan, L.; Wang, G.; Zhang, Y.; Hao, F.; Xu, R.; Zhou, L.; Liu, Z. Early dolomitization and subsequent hydrothermal modification of the middle Permian Qixia Formation carbonate in the northwest Sichuan Basin. *Geoenergy Sci. Eng.* **2023**, *221*, 211384. [CrossRef]
95. Feng, M.; Shang, J.; Shen, A.; Wen, L.; Wang, X.; Xu, L.; Liang, F.; Liu, X. Episodic hydrothermal alteration on Middle Permian carbonate reservoirs and its geological significance in southwestern Sichuan Basin, SW China. *Pet. Explor. Dev.* **2024**, *51*, 81–96. [CrossRef]
96. Li, J.; Bai, B.; Bai, Y.; Lu, X.; Zhang, B.; Qin, S.; Song, J.; Jiang, Q.; Huang, S. Fluid evolution and hydrocarbon accumulation model of ultra-deep gas reservoirs in Permian Qixia Formation of northwest Sichuan Basin, SW China. *Pet. Explor. Dev.* **2022**, *49*, 719–730. [CrossRef]
97. Chen, P.; Fu, M.; Deng, H.; Xu, W.; Wu, D.; He, P.; Guo, H. The Diagenetic Alteration of the Carbonate Rocks from the Permian Qixia Formation as Response to Two Periods of Hydrothermal Fluids Charging in the Central Uplift of Sichuan Basin, SW China. *Minerals* **2021**, *11*, 1212. [CrossRef]

98. Pan, L.; Hu, A.; Liang, F.; Jiang, L.; Hao, Y.; Feng, Y.; Shen, A.; Zhao, J. Diagenetic conditions and geodynamic setting of the middle Permian hydrothermal dolomites from southwest Sichuan Basin, SW China: Insights from in situ U–Pb carbonate geochronology and isotope geochemistry. *Mar. Pet. Geol.* **2021**, *129*, 105080. [CrossRef]
99. Di, G.; Chen, Y.; Chen, K.; Huang, Z.; Ran, Q.; Xia, Q.; Zhao, A. Distribution and activity of strike-slip faults in Gaoshiti area of Sichuan Basin and their control and significance for the development of dolomite reservoirs in Permian Qixia Formation. *Acta Pet. Sin.* **2024**, *45*, 1761–1782. (In Chinese with English Abstract)
100. Zhou, J.; Yao, G.; Yang, G.; Gu, M.; Yao, Q.; Jiang, Q.; Yang, L.; Yang, Y. Lithofacies paleogeography and favorable gas exploration zones of Qixia and Maokou Fms in the Sichuan Basin. *Nat. Gas Ind. B* **2016**, *3*, 226–233. [CrossRef]
101. Lu, F.; Tan, X.; Wang, L.; Tang, Q.; Xiao, D.; Dong, S.; Su, C.; Pan, Z. Characteristics and Controlling Factors of Dolomite Reservoirs within Shoal-controlled Karst in the Middle Permian Qixia Formation, Central Sichuan Basin. *Acta Pet. Sin.* **2021**, *39*, 456–469. (In Chinese with English Abstract)
102. Sibley, D.F.; Dedoes, R.E.; Bartlett, T.R. Kinetics of dolomitization. *Geology* **1987**, *15*, 1112–1114. [CrossRef]
103. Humphrey, E.; Gomez-Rivas, E.; Martín-Martín, J.D.; Neilson, J.; Salas, R.; Guimerà, J. Depositional and structural controls on a fault-related dolostone formation (Maestrat Basin, E Spain). *Basin Res.* **2022**, *34*, 961–990. [CrossRef]
104. Corbella, M.; Gomez-Rivas, E.; Martín-Martín, J.D.; Stafford, S.L.; Teixell, A.; Griera, A.; Travé, A.; Cardellach, E.; Salas, R. Insights to controls on dolomitization by means of reactive transport models applied to the Benicàssim case study (Maestrat Basin, eastern Spain). *Pet. Geosci.* **2014**, *20*, 41–54. [CrossRef]
105. Lucia, F.J. Rock-Fabric/Petrophysical Classification of Carbonate Pore Space for Reservoir Characterization1. *AAPG Bull.* **1995**, *79*, 1275–1300. [CrossRef]
106. Lucia, F.J. Origin and petrophysics of dolostone pore space. In *The Geometry and Petrogenesis of Dolomite Hydrocarbon Reservoirs*; Geological Society of London: London, UK, 2004.
107. Saller, A.H.; Henderson, N. Distribution of Porosity and Permeability in Platform Dolomites: Insight from the Permian of West Texas. *AAPG Bull.* **1998**, *82*, 1528–1550. [CrossRef]
108. Morrow, D.W. Distribution of Porosity and Permeability in Platform Dolomites: Insight from the Permian of West Texas: Discussion. *AAPG Bull.* **2001**, *85*, 525–529. [CrossRef]
109. Ehrenberg, S.N.; Nadeau, P.H. Sandstone vs. carbonate petroleum reservoirs: A global perspective on porosity-depth and porosity-permeability relationships. *AAPG Bull.* **2005**, *89*, 435–445. [CrossRef]
110. Li, J.; Wang, Y.; Liu, C.; Dong, D.; Gao, Z. Hydrothermal fluid activity and the quantitative evaluation of its impact on carbonate reservoirs: A case study of the Lower Paleozoic in the west of Dongying sag, Bohai Bay Basin. *Pet. Explor. Dev.* **2016**, *43*, 395–403. [CrossRef]
111. Martyushev, D.A.; Davoodi, S.; Kadkhodaie, A.; Riazi, M.; Kazemzadeh, Y.; Ma, T. Multiscale and diverse spatial heterogeneity analysis of void structures in reef carbonate reservoirs. *Geoenergy Sci. Eng.* **2024**, *233*, 212569. [CrossRef]
112. Zhang, K.; Pang, X.; Zhao, Z.; Shao, X.; Zhang, X.; Li, W.; Wang, K. Pore structure and fractal analysis of Lower Carboniferous carbonate reservoirs in the Marsel area, Chu-Sarysu basin. *Mar. Pet. Geol.* **2018**, *93*, 451–467. [CrossRef]
113. Agrawal, P.; Mascini, A.; Bultreys, T.; Aslannejad, H.; Wolthers, M.; Cnudde, V.; Butler, I.B.; Raoof, A. The impact of pore-throat shape evolution during dissolution on carbonate rock permeability: Pore network modeling and experiments. *Adv. Water Resour.* **2021**, *155*, 103991. [CrossRef]
114. Li, W.; Mu, L.; Zhao, L.; Li, J.; Wang, S.; Fan, Z.; Shao, D.; Li, C.; Shan, F.; Zhao, W.; et al. Pore-throat structure characteristics and its impact on the porosity and permeability relationship of Carboniferous carbonate reservoirs in eastern edge of Pre-Caspian Basin. *Pet. Explor. Dev.* **2020**, *47*, 1027–1041. [CrossRef]
115. Liu, J.; Pereira, G.G.; Regenauer-Lieb, K. From characterization of pore-structures to simulations of pore-scale fluid flow and the upscaling of permeability using microtomography: A case study of heterogeneous carbonates. *J. Geochem. Explor.* **2014**, *144*, 84–96. [CrossRef]
116. Mondal, I.; Singh, K.H. Understanding pore characteristics through core-based petrographic and petrophysical analysis in a heterogeneous carbonate reservoir: A case study from the Mumbai Offshore Basin, India. *Pet. Res.* **2023**, *8*, 469–480. [CrossRef]

Disclaimer/Publisher's Note: The statements, opinions and data contained in all publications are solely those of the individual author(s) and contributor(s) and not of MDPI and/or the editor(s). MDPI and/or the editor(s) disclaim responsibility for any injury to people or property resulting from any ideas, methods, instructions or products referred to in the content.